Journal of Biomolecular NMR, **22:** 225–247, 2002.
KLUWER/ESCOM

Towards high-resolution solid-state NMR on large uniformly ^{15}N- and [^{13}C,^{15}N]-labeled membrane proteins in oriented lipid bilayers

Thomas Vosegaard* & Niels Chr. Nielsen*
Laboratory for Biomolecular NMR Spectroscopy, Department of Molecular and Structural Biology, University of Aarhus, DK-8000 Aarhus C, Denmark

Received 9 October 2001; Accepted 18 December 2001

Key words: macroscopic orientation, membrane proteins, porin, rhodopsin, solid-state NMR, uniform isotope labeling

Abstract

Based on exact numerical simulations, taking into account isotropic and conformation-dependent anisotropic nuclear spin interactions, we systematically analyse the prospects for high-resolution solid-state NMR on large isotope-labeled membrane proteins macroscopically oriented in phospholipid bilayers. Using the known X-ray structures of rhodopsin and porin as models for large membrane proteins with typical α-helical and β-barrel structural motifs, the analysis considers all possible one- to six-dimensional spectra comprised of frequency dimensions with evolution under any combination of amide ^{1}H, amide ^{15}N, and carbonyl ^{13}C chemical shifts as well as ^{1}H-^{15}N dipole-dipole couplings. Under consideration of typical nuclear spin interaction and experimental line-shape parameters, the analysis provides new insight into the resolution capability and orientation-dependent transfer efficiency of existing experiments as well as guidelines as to improved experimental approaches for the study of large uniformly ^{15}N- and [^{13}C,^{15}N]-labeled membrane proteins. On basis of these results and numerical optimizations of coherence-transfer efficiencies, we propose several new high-resolution experiments for sequential protein backbone assignment and structure determination.

Introduction

Membrane proteins are responsible for most of the dynamic processes across biological membranes including ion/molecule transport, communication, and energy transduction. The biological relevance of membrane proteins is emphasized in recent statistical analyses of the genomes for several organisms. They indicate that about 30% of all open reading frames encode helix-bundle membrane proteins (Wallin and von Heijne, 1998; Arkin et al., 1998). Indeed membrane proteins also have great commercial interest as evidenced by the fact that G-protein coupled receptors (GPCRs) and ion-channels currently comprise more than 50% of the human drug targets (Russell and Eggleston, 2000).

*To whom correspondence should be addressed. E-mails: ncn@imsb.au.dk; tv@imsb.av.dk

The high throughput by systematic structural genomics, currently with approximately four hundred new XRD protein structures and hundred liquid-state NMR structures released on the PDB server (Bernstein et al., 1977) every year, is in striking contrast to the fact that less than fifty structures are known for membrane proteins (Preusch et al., 1998; White and Wimley, 1999). For XRD difficulties in crystallizing membrane proteins in a lipid environment represent the major obstacle, whereas the success of liquid-state NMR studies is limited by long correlation times for most proteins incorporated into phospholipid vesicles or bilayers. Confronted with these problems, a major effort has recently been devoted to establishing solid-state NMR as a tool to obtain atomic-resolution structure information for proteins immobilized by membrane association (Opella, 1997; Griffin, 1998). This has led to numerous studies which, through orientation-dependent interactions as well as

accurate distance and torsion-angle measurements for specific atoms in selectively isotope-labeled samples, have provided valuable information about membrane-associated helix conformation (Opella et al., 1999; Kovacs et al., 2000; Bak et al., 2001b), multimerization (Fu et al., 2000), and ligand-receptor interactions (Middleton et al., 2000; Appleyard et al., 2000). While this fragmentary approach has proven useful for the establishment of new experimental methods and specific structure information, it is clearly tedious and expensive for complete structure determination, not least considering the need for multiple samples with different isotope labeling pattern. With this aspect in mind several studies have recently addressed uniformly ^{13}C- and ^{15}N-labeled peptides and small proteins in non-oriented (McDermott et al., 2000; Pauli et al., 2001; Egorova-Zachernyuk et al., 2001; Detken et al., 2001) and uniaxially oriented samples (Ketchem and Cross, 1993; Marassi et al., 1997; Opella et al., 1999).

Although uniform labeling is attractive from a practical point-of-view, it clearly introduces new problems with respect to spectral resolution being particularly pronounced for large proteins. For high-resolution magic-angle-spinning (MAS) spectra, this is mainly ascribed to the relatively narrow isotropic chemical shift range matching unfavorably with the presence of many resonances and the relatively large line widths typically observed in solid-state NMR spectra. This applies in particular for membrane-associated proteins for which favorable homogeneous, microcrystalline sample conditions (Pauli et al., 2001; Detken et al., 2001) will generally not be achievable (Pauli et al., 2000). With such aspects in mind, Tycko (1996) used numerical simulations to predict that it should be possible to make complete backbone resonance assignments in multiple-dimensional MAS powder spectra of proteins with up to 50–100 residues. This statement has recently been corroborated experimentally by McDermott et al. (2000) and Pauli et al. (2001) who demonstrated partial or full backbone resonance assignments for microcrystalline samples of the 58-residue BPTI and the 62-residue α-spectrin SH3 domain, respectively.

In an alternative experimental approach using macroscopic orientation of the membrane proteins in phospholipid bilayers (Opella, 1997), the unfavorable isotropic shift-range versus line-width mismatch of MAS methods may partially be alleviated by exploiting resonance dispersion through *anisotropic* nuclear spin interactions. Thus, although oriented samples typically show slightly larger line widths than rotating samples, the frequency dispersion offered by anisotropic chemical shift and dipole-dipole coupling interactions may allow for complete backbone assignment of uniformly ^{15}N-labeled proteins significantly larger than 50 residues as predicted by Marassi et al. (1997). Assisted by additional uniform ^{13}C labeling, it may be possible to resolve resonance from more than 100 residues using 3D correlation experiments (Ishii and Tycko, 2000). In this context it is relevant to note that the oriented-sample NMR experiments, in addition to improved resonance dispersion, offer directly accessible structure information. Upon assignment the resonance positions or resonance patterns immediately provide detailed information about the local molecular structure as well as the long-range tertiary structure and the overall conformation of the molecule in the lipid bilayer.

Considering the acute need for methods which allow atomic-resolution structure determination of membrane proteins and the promising features of macroscopic-oriented sample methods, we will in this paper analyse the potential of such methods for the study of large uniformly ^{15}N- and [^{13}C,^{15}N]-labeled membrane proteins. This analysis will be conducted numerically using the SIMPSON (Bak et al., 2000) simulation package along with the recent SIMMOL program (Bak et al., 2002) allowing straightforward association of realistic anisotropic tensor information to the three-dimensional structure of proteins. Equipped with these tools, we systematically investigate the potential of essentially all possible one- to six-dimensional NMR experiments for resolution and excitation of signals required for full assignment of backbone atoms of typical α-helical and β-barrel type proteins in the 35-40 kDa regime.

Materials and methods

Atomic coordinates for the structures of rhodopsin (Palczewski et al., 2000) and porin (Weiss et al., 1991; Weiss and Schulz, 1992) have been achieved from the PDB (Bernstein et al., 1977) files 1F88 and 2POR, respectively. Rhodopsin has seven trans-membrane α-helices spanning residues Trp_{35}-Gln_{65}, Pro_{71}-His_{100}, Pro_{107}-Val_{139}, Asn_{151}-Val_{173}, Asn_{200}-Gln_{225}, Glu_{247}-Thr_{277}, and Ile_{286}-Tyr_{306} (Palczewski et al., 2000). The trans-membrane part of porin is a sixteen-stranded β-barrel which spans residues Glu_1-Asn_{15}, Asp_{18}-Thr_{35}, Leu_{39}-Lys_{46}, Gly_{59}-Gly_{65},

Gly_{68}-Asp_{74}, Val_{118}-Ala_{125}, Phe_{128}-Ser_{135}, Gln_{148}-Phe_{158}, Tyr_{161}-Asp_{171}, Met_{181}-Phe_{192}, Thr_{195}-Leu_{206}, Val_{227}-Phe_{240}, Thr_{243}-Ile_{254}, Asp_{258}-Leu_{271}, Als_{275}-Asp_{285}, and Val_{292}-Phe_{301} (Weiss et al., 1991; Weiss and Schulz, 1992). The proteins are assumed to align in the lipid bilayers with the average C_i^α-C_{i+1}^α vectors (i runs through all the membrane-spanning segments) parallel to the membrane normal.

All analyses of the protein structures are performed using our recently developed SIMMOL software (Bak et al., 2002) on a 500 MHz Pentium/Linux 2.4 laptop. SIMMOL provides a Tcl-controlled interface which facilitates establishing the orientation of the NMR tensors for different residues in the proteins. Simulations of NMR spectra are either performed directly using SIMMOL or by its companion SIMPSON (Bak et al., 2000) when effects from multiple spin-systems and/or finite rf pulses need to be taken into account. SIMMOL calculation of the resonance positions in 2D spectra for rhodopsin or porin last approximately 5 s, whereas the four-spin SIMPSON simulations of the selective coherence-transfer efficiencies including, finite-pulse and off-resonance effects last approximately 15 s for the full ∼300 residue structures. Prior to simulation of the effective ^{1}H-^{15}N dipolar couplings in rhodopsin, amide-proton coordinates have been added to the rhodopsin structure employing the SIMMOL defaults for the H-N bond length (1.07Å) and H-N-C$^\alpha$bond angle (114°).

Results and discussion

NMR interactions of the backbone atoms

While dispersion of resonances through anisotropic interactions may be favorable from a resolution point-of-view, it is important to keep in mind that this is achieved at the expense of information about residue type and secondary-structure predictions from isotropic nuclear spin interactions (Wishart and Sykes, 1994; Cornilescu et al., 1999; Luca et al., 2001). Considering the chemical shift interaction, the resonance position in oriented samples reflects five parameters describing the magnitude and orientation of the chemical shift tensor relative to the external magnetic field rather than the isotropic chemical shift alone as obtained under high-resolution MAS conditions. This intuitive disadvantage may, however, be very useful considering that the chemical shift tensors for most peptide backbone atoms largely possess the same magnitude and orientation relative to the peptide plane (see Figure 1a), independently on the residue type and the secondary structure of the peptide (Opella et al., 1987; Cross and Quine, 2000). This implies that the resonance position to a good approximation relates directly to two Euler angles orienting the peptide plane relative to the external magnetic field. Thereby, it is possible not only to obtain information about the structure of the protein but also its conformation and orientation relative to, e.g., the bilayer normal in samples macroscopically oriented with this axis parallel to the external magnetic field. Obviously, a prerequisite is that the relevant resonances can be resolved and assigned unambiguously.

The fact that most peptide-backbone anisotropic interaction tensors to a good approximation are uniquely related to the peptide plane opens the possibility for accurately taking these interactions into account in numerical simulations of solid-state NMR spectra for oriented membrane proteins. In the following we will exploit this feature to numerically predict the resolution capability and sensitivity of multi-dimensional correlation experiments. For this purpose, Table 1 summarizes typical parameters for the magnitude and orientation of relevant interaction tensors involving the amide ^{1}H (1, a), amide ^{15}N (2, b), and carbonyl ^{13}C′(4, 5, c) chemical shifts as well as ^{1}H-^{15}N dipole-dipole couplings (3), where the parentheses contain identification codes used henceforth for labeling of correlations, pulse sequences, and pulse-sequence elements. Frequency dimensions reflecting chemical shift evolution under ^{13}C$^\alpha$ and side-chain ^{13}C atoms are not considered since they generally exhibit strong dependency on the residue type and the secondary structure, while frequency-encoding by evolution under ^{13}C-^{13}C and ^{13}C-^{15}N dipole-dipole couplings are disregarded because of their relatively small magnitudes. For clarification Figure 1b shows a schematic of a peptide chain highlighting the above-mentioned atoms with their interaction tensors attached to the peptide plane. It is assumed that any of the interactions in Table 1 may be observed either directly or indirectly in a multi-dimensional NMR experiment with each frequency dimension directly related to one of the interactions. In this context it is relevant to point out that the ^{13}C$^\alpha$ and side-chain ^{13}C atoms are assumed not to appear in the carbonyl region of the ^{13}C spectrum. For ^{13}C$^\alpha$ this is plausible since the powder pattern associated with the typical ^{13}C$^\alpha$ chemical shift parameters $\delta_{iso} = 50$ ppm, $\delta_{aniso} = -20$ ppm, $\eta = 0.43$ (Naito et al., 1981) will not overlap with the ^{13}C′ powder pattern corresponding to

Table 1. Different frequency dimensions with associated anisotropic tensor parameters, typical spectral windows, and proposed sampling conditions (for indirect detection) used in the present work[a]

ID	Dimension	δ_{iso}	δ_{aniso}	η	$b_{IS}/2\pi$	Ω_{PE}	$\Delta\nu_{1/2}$	sw[b]	N[c]	Reference
1	^1H_i shift	9.3	7.7	0.65	–	(90,−90,90)	1	16(13)	16(13)	Wu et al. (1995)
a	$^1H_{i-1}$,$^1H_{i+1}$ shifts	9.3	7.7	0.65	–	(90,−90,90)	1	16(13)	16(13)	
2	$^{15}N_i$ shift	119	97.7	0.13	–	(−90,−90,−17)	3	110	37	Teng et al. (1992), Wu et al. (1995), Tan et al. (1999)
b	$^{15}N_{i-1}$,$^{15}N_{i+1}$ shifts	119	97.7	0.13	–	(−90,−90,−17)	3	110	37	
3	^1H_i-$^{15}N_i$ dipole	–	–	–	9.9	(0,90,0)	3	20	67	Wu et al. (1995)
4	$^{13}C'_i$ shift	170	−82	0.80	–	(0,0,94)	3	250(148)	83(49)	Teng et al. (1992), Weliky and Tycko (1996), Tan et al. (1999)
5	$^{13}C'_{i-1}$ shift	170	−82	0.80	–	(0,0,94)	3	250(148)	83(49)	
c	$^{13}C'_{i-1}$,$^{13}C'_{i+1}$ shifts	170	−82	0.80	–	(0,0,94)	3	250(148)	83(49)	

[a]δ_{iso} is the isotropic chemical shift (ppm), δ_{aniso} the chemical shift anisotropy (ppm), η the chemical shift asymmetry parameter, $b_{IS}/2\pi$ the dipolar coupling (kHz), and Ω_{PE} the principal-axis (P) to peptide-plane (E) Euler angles (in degrees). $\Delta\nu_{\frac{1}{2}}$ represents the typical line width (ppm for shift, kHz for coupling) for the relevant dimension. For indirect detection we propose a minimal spectral width sw (in ppm or kHz) and number of increments N. The identification (ID) codes refer to the labeling in Figure 1.

[b]For the ^{15}N chemical-shift and ^1H-^{15}N dipole-dipole interactions the spectral width (sw) equals the span of the interaction: $\delta_{aniso}(1+\eta)$ for the chemical shift and $2b_{IS}/2\pi$ for the dipolar coupling. For the ^1H and ^{13}C chemical shift interactions the spectral width should cover the range from ∼0 ppm to ∼15 ppm and ∼240 ppm, respectively, to avoid extensive artificial peaks from other spins folding into the desired spectral region. In parentheses are given the span of the desired tensors.

[c]The proposed number of increments (N) needed for indirect detection is calculated as $N = sw/\Delta\nu_{1/2}$ which ensures that truncation of the FID adds less than 7% to the line width for a Lorentzian line. The parentheses include numbers of increments corresponding to the minimal spectral width defined by the span of the interaction.

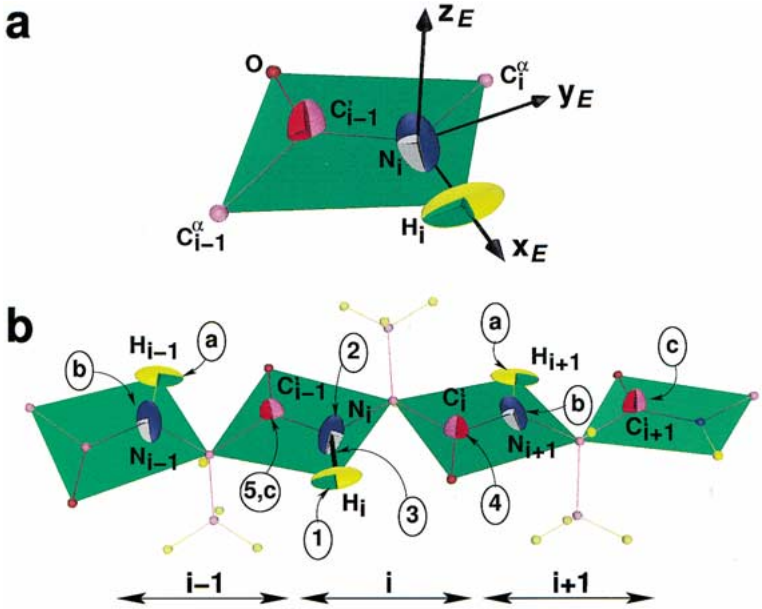

Figure 1. (a) Graphical SIMMOL representation of the ^{1}H, ^{15}N, and ^{13}C′chemical shift tensor ellipsoids within the peptide plane. x_E, y_E, and z_E define the peptide-plane coordinate system E. (b) Visualization of a SIMMOL generated three-residue $(i-1, i, i+1)$ alanine peptide chain with labeling of the interactions listed in Table 1.

the parameters in Table 1. We note that Figure 1b distinguishes between chemical shifts assumed accessible by selective/specific coherence transfer (numbers) and 'symmetrically' disposed chemical shifts being accessible through non-selective/non-specific coherence transfer (letters), e.g., using proton-mediated spin-diffusion (Szeverenyi et al., 1982).

To provide a reasonable evaluation of the practically achievable resolution capability, Table 1 contains conservative estimates on the line widths being realistic to observe in experimental spectra according to previous studies of single crystals or uniaxially oriented samples as summarized in Table 2. Obviously, taken into combination with the typical nuclear spin interaction parameters these line widths provide additional important information about the optimum sample conditions and thereby about which interactions should most conveniently be probed in the direct detection dimension. Thus, for the convenience of the reader Table 1 also includes proposed spectral widths (sw) and numbers of sampling points (N) calculated as $N = sw/\Delta\nu_{1/2}$. The latter number ensures that truncation of the FID increases the line width by less than 7%. We note that this additional line broadening may already be part of the experimental line width estimates in Table 2 and may depend on whether the interaction is sampled indirectly or directly. This issue is not included in the following evaluation of the resolution power.

Model structures

With large membrane-spanning proteins being the target of our study, we have chosen recent X-ray structures for rhodopsin (Figure 2a) and porin (Figure 2b) as representative models for the two known membrane-spanning structural motifs for membrane proteins, namely trans-membrane (TM) α-helices and β-barrels (White and Wimley, 1999). Specifically, we have for rhodopsin, which is a GPCR containing seven TM α-helices, chosen the recent X-ray structure of Palczewski et al. (2000) while the X-ray structure of Weiss et al. (1991) was chosen for the sixteen-stranded β-barrel porin. Both proteins contain approximately 300 residues and are thereby significantly larger than any protein whose structure has been determined by solid-state NMR so far. Equipped with these large, albeit typical, structures, the typical peptide nuclear spin interaction parameters, and experimentally achievable line widths in Table 1, it is possible to systematically investigate the performance of essentially any kind of solid-state NMR experiment using the recently developed SIMMOL (Bak et al., 2002) and SIMPSON (Bak et al., 2000) software packages. SIMMOL allows automatic establishment of all relevant anisotropic tensor

Table 2. Typical line widths observed for ^{1}H, ^{15}N, and $^{13}C'$ chemical shifts and ^{1}H-^{15}N dipolar couplings in various samples[a]

Dimension	$\Delta\nu_{1/2}$	Sample	Reference
^{1}H (1,a)	1.2	fd coat protein (oriented bilayer)	Marassi et al. (1997)
	0.8	N-acetylleucine (single crystal)	Ramamoorthy et al. (1999)
^{15}N (2,b)	3	fd coat protein (oriented bilayer)	Marassi et al. (1997)
	2–3	N-acetylglycine (single crystal)	Gu and Opella (1999a)
	1–3	N-acetylleucine (single crystal)	ramamoorthy et al. (1999)
	3	magainin/Vpu (oriented bilayer)	Marassi et al. (2000)
	2.5	Alanylglycylglycine (single crystal)	Ishii and Tycko (2000)
^{1}H-^{15}N (3)	0.3	fd coat protein (oriented bilayer)	Marassi et al. (1997)
	0.4	N-acetylglycine (single crystal)	Gu and Opella (1999a)
	0.2	N-acetylleucine (single crystal)	Ramamoorthy et al. (1999)
	0.25	magainin/Vpu (oriented bilayer)	Marassi et al. (2000)
$^{13}C'$(4,5,c)	2.4–4.2[b]	Alanylglycylglycine (single crystal)	Ishii and Tycko (2000)
	2–4	N-acetylglycine/*N*-acetylvaline (single crystal)	Gu and Opella (1999a, 1999b)

[a]The line width ($\Delta\nu_{\frac{1}{2}}$; full width at half height) is given in ppm for shifts and kHz for dipolar couplings.

[b]The typical line widths of 2–3.5 ppm reported have been multiplied by 1.2 to account for chemical shift scaling.

information and simulation of ideal solid-state NMR spectra without consideration of features such as non-ideal coherence/population transfer, finite rf pulses, multiple-spin effects etc. SIMPSON allows all these features to be taken explicitly into account while using tensor parameters issued by SIMMOL.

Resolution power of multidimensional correlation experiments

Figure 2 shows 1D ^{15}N NMR spectra of uniaxially oriented rhodopsin and porin simulated with SIMMOL using a typical 3 ppm line width (c,d) and infinitely sharp lines (e,f). Considering that the spectra contain about 300 resonances of 3 ppm line width within a 100 ppm chemical shift range, it is not surprising that the 1D spectra do not provide sufficient resolution to give structural information beyond the expected down-field dominance for the largely trans-membrane α-helical rhodopsin and a corresponding up-field dominance for the trans-membrane β-barrel in porin. To alleviate this resolution problem and to establish complementary structure information from ^{1}H-^{15}N dipolar couplings, it has become popular to use the so-called polarization inversion spin exchange at the magic angle (PISEMA) experiment proposed by Opella and co-workers (Wu et al., 1994). The relevance of this approach in the studies of large membrane proteins becomes evident from Figures 2g and 2h showing SIMMOL simulated PISEMA spectra of rhodopsin and porin, with resolved and unresolved resonances represented by open and filled ellipses, respectively, with a size reflecting the typical line widths in Table 1. These spectra clearly corroborate the resolution-wise attractive features of 2D PISEMA spectra even for quite large proteins, although it is also evident that substantial overlap remains in the most crowded regions of the ^{15}N spectrum. This opens some very interesting questions. How good is the actual resolution in the PISEMA spectra and would there be better alternatives for large uniformly ^{15}N- or [^{13}C,^{15}N]-labeled membrane proteins?

To answer these questions, we need a unique definition of the achievable resolution in the various possible frequency dimensions of multiple-dimensional NMR experiments using the interaction/frequency dimensions and typical line-shape parameters listed in Table 1. Within the assumption that all resonances in a given frequency dimension i have identical line widths, $\Delta\nu_{1/2}(i)$, it proves convenient to use normalized frequencies $x(i) = \nu(i)/\Delta\nu_{1/2}(i)$ with unit line widths, where $\nu(i)$ is the frequency in normal units (ppm or Hz). In this case an N-dimensional Lorentzian line for a given resonance a may be expressed as (Ernst et al., 1987)

$$\mathcal{S}_a(\mathbf{x}) = \prod_{i=1}^{N} \frac{1}{1 + 4(x(i) - x_a(i))^2}, \tag{1}$$

with $x_a(i) = \nu_a(i)/\Delta\nu_{1/2}(i)$ denoting the normalized resonance frequency in the i'th spectral dimension. Using this notation, two resonances may be considered

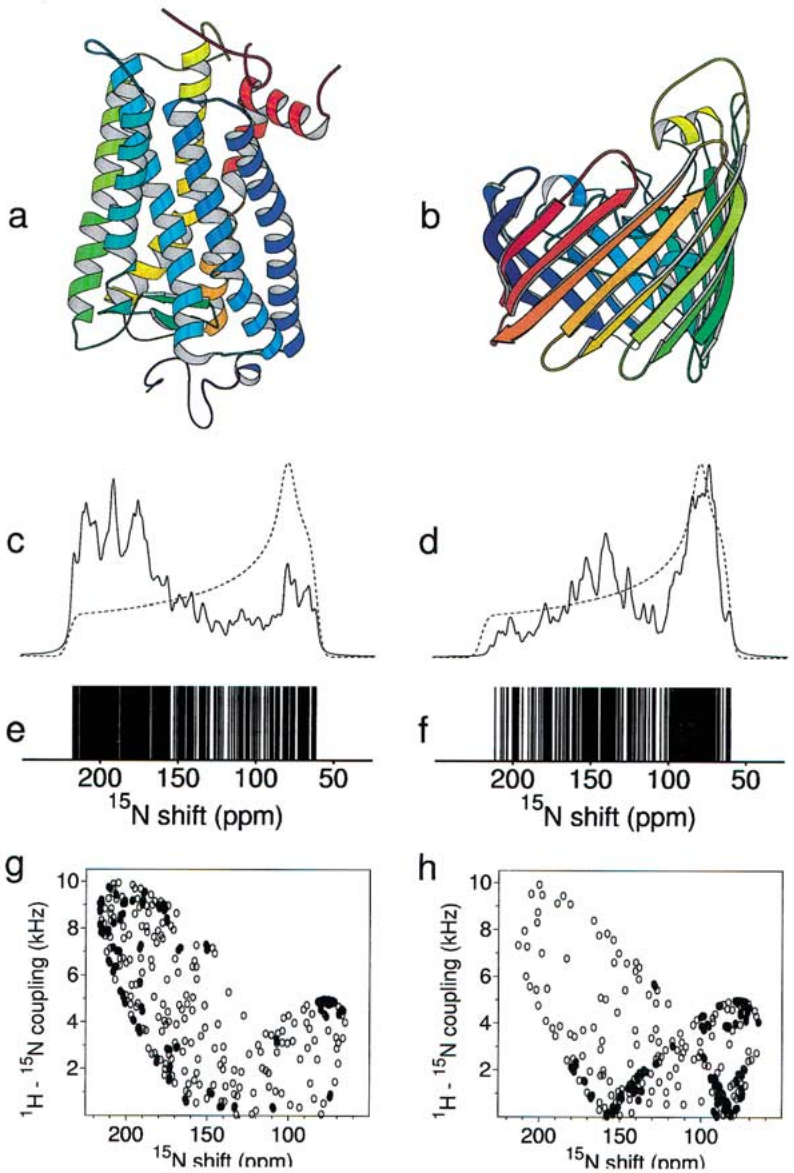

Figure 2. Molecular structures of (a) rhodopsin and (b) porin along with SIMMOL simulated NMR spectra of rhodopsin (c,e,g) and porin (d,f,h) macroscopically oriented with the average α-helix (rhodopsin) and β-strand (porin) axes parallel to the external magnetic field. The simulated 1D ^{15}N spectra (solid lines in (c,d)) employ 3 ppm line width for all resonances and are overlaid by a simulated powder spectrum (dashed lines) employing the parameters from Table 1. (e,f) Stick plots of the resonance positions from (c,d). (g,h) Simulated PISEMA spectra with open and closed ellipses representing resolved and unresolved resonances, respectively. The size of the ellipses correspond to typical line widths of 0.3 kHz and 3 ppm for the ^{1}H-^{15}N dipole coupling and ^{15}N chemical shift dimensions, respectively.

resolved if there is a 'valley' between the two resonances in the summed $\mathcal{S}_a + \mathcal{S}_b$ spectrum. In a normal one-dimensional representation this corresponds to the existence of a zero crossing for $\partial^2(\mathcal{S}_a(x)+\mathcal{S}_b(x))/\partial x^2$ in the interval between x_a and x_b. This occurs only if $|x_a - x_b| \geq 1/\sqrt{3}$. Although the minimum distance to achieve resolution of two lines in multi-dimensional spectra may be slightly smaller depending on the orientation of the vector $\mathbf{x}_a - \mathbf{x}_b$, we conservatively define two resonances as being resolved when $|\mathbf{x}_a - \mathbf{x}_b| > \frac{1}{\sqrt{3}}$ implying

$$\sum_{i=1}^{N} \left(\frac{\nu_a(i) - \nu_b(i)}{\Delta\nu_{\frac{1}{2}}(i)} \right)^2 > \frac{1}{3} \quad . \tag{2}$$

Thus, in a spectrum containing multiple lines, a particular resonance a is considered resolved provided it fulfills the inequality in Equation 2 for all other resonances b ($b \neq a$). Using this definition, the 1D spectra in Figures 2c and 2d may readily evaluated to allow resolution of less than 1% of the resonances for uniformly ^{15}N-labeled rhodopsin and porin, while the corresponding PISEMA spectra in Figures 2g and 2h allow for resolution of 59% of the resonances for rhodopsin and 48% of the resonances for porin.

Using the same approach, it is straightforward to systematically analyse the resolution power for any type of one- to six-dimensional solid-state NMR experiments allowing the interactions listed in Table 1 to be observed in separate spectral dimensions. The results of such an analysis on the rhodopsin and porin structures are given in Table 3, where the columns for the various multiple-dimensional experiments contain the number (fraction) of resolved resonances for rhodopsin and porin. It should be noted that we, to avoid unfavorable distribution of the initial coherence to an excessively large number of spins, restricted ourselves to experiments with only one non-selective transfer step (i.e., at maximum one of the frequency dimensions labeled a, b, or c in Table 1). Table 3 clearly supports the trend already established from Figure 2, namely that 1D experiments do not provide any resolution for large membrane proteins, while the situation is markedly improved just going to 2D correlation experiments. It is, however, also clear that there is a substantial variation in the resolution power of 2D experiments ranging from 5% to about 80% depending on which interactions are correlated and which of the two compounds is under consideration. Using 3D experiments, it appears possible to resolve essentially all resonances, which obviously also applies for higher-dimensional approaches. Considering the quite large variation in the resolution power, in particular for the practically most relevant 2D and 3D approaches, it is evident that the present analysis may provide useful guidelines for the evaluation and development of experiments for solid-state NMR on uniaxially oriented proteins.

Before entering a detailed discussion of specific experiments, it is relevant to point out some general features observed from Table 3. First, we note that the ^{1}H chemical shift dimension generally contributes only little resolution power for the present model systems as compared to the other interactions. This is not surprising considering the relatively small dispersion of the anisotropic amide ^{1}H chemical shifts ($\approx$ 13 ppm) relative to the typical line width (1 ppm). It should be noted, however, that ^{1}H chemical shifts have proven useful for resolution of resonances from *in-plane* α-helices (Marassi et al., 2000) being the least favorable case for the PISEMA experiment. Second, it is evident from Table 3 that correlations between different peptide planes generally provide superior resolution than correlations within the same peptide plane. An example would be the 3D intra-residue [$^{1}H_i$-$^{15}N_i$ dipole coupling, $^{15}N_i$ shift, $^{13}C'_i$ shift] correlation experiment (labeled 2-3-4 in Table 3), which for both compounds improves the resolution by about 25% compared to the intra-residue [$^{1}H_i$-$^{15}N_i$ dipole coupling, $^{15}N_i$ shift, $^{13}C'_{i-1}$ shift] correlation experiment (labeled 2-3-5 in Table 3).

Practical implementation of multiple-dimensional correlation experiments

The resolution power is obviously not the only criterion for selecting a given multi-dimensional correlation experiment. It is necessary to combine this information with the practical feasibility of the experiment seen in relation to the underlying coherence-transfer processes, the required isotope-labeling procedures, and the performance of currently available pulse-sequence elements. With respect to isotope labeling, it is most relevant to discriminate between uniform ^{15}N labeling and uniform [^{13}C,^{15}N] labeling, e.g., considering that NMR experiments for purely ^{15}N-labeled proteins may be conducted on standard double-resonance equipment rather than on more advanced triple-resonance instrumentation. Accordingly, the vast majority of solid-state NMR studies of macroscopically oriented peptides have so far relied on [^{1}H,^{15}N] double-resonance experiments on ^{15}N-labeled peptides/proteins. Another important aspect to address is the orientation dependence of the dipolar couplings which typically are used for practical realization of the coherence transfers required to correlate the various interactions. In contrast to powder samples, variations in the effective dipolar couplings may lead to non-uniform excitation profiles causing potential loss of signals during the fundamental coherence-transfer processes.

Double-resonance experiments

Considering 2D [^{1}H,^{15}N] double-resonance experiments, Table 3 reveals that most resolution power is offered by the 2–3, 2-b, and 3-b experiments correlating the ^{1}H-^{15}N dipole coupling with the direct

Table 3. Calculated number (and percentage) of resolved resonances from multi-dimensional NMR spectra of rhodopsin and porin using uniform ^{15}N, ^{13}C, or [^{13}C,^{15}N] labeling depending on the involved interactions[a]

Number of	$^{1}H_i$	$^{1}H_{i\pm1}$	$^{15}N_i$	$^{1}H_i-^{15}N_i$	$^{15}N_{i\pm1}$	$^{13}C'_i$	$^{13}C'_{i-1}$	$^{13}C'_{i\pm1}$	Resolved resonances	
Dimensions	1	a	2	3	b	4	5	c	Rhodopsin	Porin
1	1	–	–	–	–	–	–	–	0 (0%)	0 (0%)
	–	–	2	–	–	–	–	–	1 (0%)	3 (1%)
	–	–	–	3	–	–	–	–	0 (0%)	3 (1%)
	–	–	–	–	–	4	–	–	2 (1%)	1 (0%)
2	1	a	–	–	–	–	–	–	16 (5%)	16 (5%)
	1	–	2	–	–	–	–	–	83 (26%)	95 (32%)
	1	–	–	3	–	–	–	–	50 (16%)	57 (19%)
	1	–	–	–	b	–	–	–	84 (26%)	82 (28%)
	1	–	–	–	–	4	–	–	117 (37%)	131 (44%)
	1	–	–	–	–	–	5	–	75 (24%)	96 (33%)
	1	–	–	–	–	–	–	c	45 (14%)	48 (16%)
	–	a	2	–	–	–	–	–	86 (26%)	89 (30%)
	–	a	–	3	–	–	–	–	42 (13%)	54 (18%)
	–	a	–	–	–	4	–	–	44 (13%)	69 (23%)
	–	a	–	–	–	–	5	–	80 (24%)	95 (32%)
	–	–	2	3	–	–	–	–	187 (59%)	141 (48%)
	–	–	2	–	b	–	–	–	194 (58%)	186 (62%)
	–	–	2	–	–	4	–	–	247 (73%)	222 (74%)
	–	–	2	–	–	–	5	–	181 (54%)	213 (71%)
	–	–	2	–	–	–	–	c	145 (43%)	156 (52%)
	–	–	–	3	b	–	–	–	178 (56%)	125 (42%)
	–	–	–	3	–	4	–	–	219 (69%)	204 (69%)
	–	–	–	3	–	–	5	–	169 (53%)	182 (62%)
	–	–	–	3	–	–	–	c	124 (39%)	122 (41%)
	–	–	–	–	b	4	–	–	153 (45%)	156 (52%)
	–	–	–	–	b	–	5	–	206 (61%)	168 (56%)
	–	–	–	–	–	4	5	–	216 (64%)	237 (79%)
	–	–	–	–	–	4	–	c	153 (45%)	191 (64%)
3	1	a	2	–	–	–	–	–	220 (69%)	220 (75%)
	1	a	–	3	–	–	–	–	184 (58%)	203 (69%)
	1	a	–	–	–	4	–	–	214 (68%)	228 (77%)
	1	a	–	–	–	–	5	–	187 (59%)	233 (79%)
	1	–	2	3	–	–	–	–	213 (67%)	174 (59%)
	1	–	2	–	b	–	–	–	288 (91%)	261 (88%)
	1	–	2	–	–	4	–	–	285 (90%)	277 (94%)
	1	–	2	–	–	–	5	–	200 (63%)	225 (76%)
	1	–	2	–	–	–	–	c	194 (61%)	211 (72%)
	1	–	–	3	b	–	–	–	264 (83%)	246 (83%)
	1	–	–	3	–	4	–	–	276 (87%)	268 (91%)
	1	–	–	3	–	–	5	–	179 (56%)	213 (72%)
	1	–	–	3	–	–	–	c	177 (56%)	195 (66%)
	1	–	–	–	b	4	–	–	263 (83%)	274 (93%)
	1	–	–	–	b	–	5	–	263 (83%)	258 (87%)
	1	–	–	–	–	4	5	–	272 (86%)	280 (95%)
	1	–	–	–	–	4	–	c	255 (80%)	273 (93%)

Table 3 continued.

Number of Dimensions	$^{1}H_i$ 1	$^{1}H_{i\pm1}$ a	$^{15}N_i$ 2	$^{1}H_i$—$^{15}N_i$ 3	$^{15}N_{i\pm1}$ b	$^{13}C'_i$ 4	$^{13}C'_{i-1}$ 5	$^{13}C'_{i\pm1}$ c	Resolved resonances Rhodopsin	Porin
	–	a	2	3	–	–	–	–	271 (85%)	248 (84%)
	–	a	2	–	–	4	–	–	287 (85%)	274 (91%)
	–	a	2	–	–	–	5	–	266 (79%)	281 (94%)
	–	a	–	3	–	4	–	–	277 (87%)	260 (88%)
	–	a	–	3	–	–	5	–	263 (83%)	270 (92%)
	–	a	–	–	–	4	5	–	278 (82%)	274 (91%)
	–	–	2	3	b	–	–	–	305 (96%)	264 (89%)
	–	–	2	3	–	4	–	–	313 (99%)	285 (97%)
	–	–	2	3	–	–	5	–	247 (78%)	240 (81%)
	–	–	2	3	–	–	–	c	245 (77%)	225 (76%)
	–	–	2	–	b	4	–	–	321 (95%)	292 (97%)
	–	–	2	–	b	–	5	–	319 (95%)	286 (95%)
	–	–	2	–	–	4	5	–	319 (95%)	294 (98%)
	–	–	2	–	–	4	–	c	317 (94%)	292 (97%)
	–	–	–	3	b	4	–	–	307 (97%)	286 (97%)
	–	–	–	3	b	–	5	–	298 (94%)	281 (95%)
	–	–	–	3	–	4	5	–	305 (96%)	290 (98%)
	–	–	–	3	–	4	–	c	304 (96%)	285 (97%)
	–	–	–	–	b	4	5	–	321 (95%)	293 (98%)
4	1	a	2	3	–	–	–	–	282 (89%)	263 (89%)
	1	a	2	–	–	4	–	–	303 (96%)	289 (98%)
	1	a	2	–	–	–	5	–	268 (85%)	280 (95%)
	1	a	–	3	–	4	–	–	302 (95%)	289 (98%)
	1	a	–	3	–	–	5	–	265 (84%)	279 (95%)
	1	a	–	–	–	4	5	–	299 (94%)	289 (98%)
	1	–	2	3	b	–	–	–	309 (97%)	273 (93%)
	1	–	2	3	–	4	–	–	315 (99%)	287 (97%)
	1	–	2	3	–	–	5	–	247 (78%)	240 (81%)
	1	–	2	3	–	–	–	c	247 (78%)	230 (78%)
	1	–	2	–	b	4	–	–	313 (99%)	293 (99%)
	1	–	2	–	b	–	5	–	303 (96%)	283 (96%)
	1	–	2	–	–	4	5	–	309 (97%)	291 (99%)
	1	–	2	–	–	4	–	c	309 (97%)	289 (98%)
	1	–	–	3	b	4	–	–	311 (98%)	293 (99%)
	1	–	–	3	b	–	5	–	298 (94%)	283 (96%)
	1	–	–	3	–	4	5	–	305 (96%)	291 (99%)
	1	–	–	3	–	4	–	c	305 (96%)	289 (98%)
	1	–	–	–	b	4	5	–	311 (98%)	293 (99%)
	–	a	2	3	–	4	–	–	315 (99%)	291 (99%)
	–	a	2	3	–	–	5	–	293 (92%)	283 (96%)
	–	a	2	–	–	4	5	–	327 (97%)	296 (99%)
	–	a	–	3	–	4	5	–	311 (98%)	293 (99%)
	–	–	2	3	b	4	–	–	317 (100%)	293 (99%)
	–	–	2	3	b	–	5	–	311 (98%)	283 (96%)
	–	–	2	3	–	4	5	–	315 (99%)	291 (99%)
	–	–	2	3	–	4	–	c	315 (99%)	289 (98%)
	–	–	2	–	b	4	5	–	335 (99%)	298 (99%)
	–	–	–	3	b	4	5	–	315 (99%)	293 (99%)

Table 3 continued.

Number of Dimensions	^1H_i 1	$^1H_{i\pm1}$ a	$^{15}N_i$ 2	^1H_i–$^{15}N_i$ 3	$^{15}N_{i\pm1}$ b	$^{13}C'_i$ 4	$^{13}C'_{i-1}$ 5	$^{13}C'_{i\pm1}$ c	Resolved resonances Rhodopsin	Porin
5	1	a	2	3	–	4	–	–	315 (99%)	293 (99%)
	1	a	2	3	–	–	5	–	295 (93%)	283 (96%)
	1	a	2	–	–	4	5	–	311 (98%)	293 (99%)
	1	a	–	3	–	4	5	–	311 (98%)	293 (99%)
	1	–	2	3	b	4	–	–	317 (100%)	293 (99%)
	1	–	2	3	b	–	5	–	311 (98%)	283 (96%)
	1	–	2	3	–	4	5	–	315 (99%)	291 (99%)
	1	–	2	3	–	4	–	c	315 (99%)	289 (98%)
	1	–	2	–	b	4	5	–	315 (99%)	293 (99%)
	1	–	–	3	b	4	5	–	315 (99%)	293 (99%)
	–	a	2	3	–	4	5	–	315 (99%)	293 (99%)
	–	–	2	3	b	4	5	–	317 (100%)	293 (99%)
6	1	a	2	3	–	4	5	–	315 (99%)	293 (99%)
	1	–	2	3	b	4	5	–	317 (100%)	293 (99%)

[a]The calculations are based on the typical line shape and nuclear spin parameters in Table 1. Note that only frequency dispersion from anisotropic spin interactions is considered.

(2-3) or remote (3-b) ^{15}N chemical shift, and direct to remote ^{15}N chemical shift (2-b). The first of these experiments, 2–3, may be conducted using the well-established PISEMA pulse sequence (Wu et al., 1994) shown in Figure 3a allowing resolution of about 50–60% of the resonances for the two 35–40 kDa model proteins. The PISEMA pulse sequence is experimentally attractive in the sense that it through non-selective excitation of ^{15}N coherence using cross-polarization (CP) (Pines et al., 1973) from the surrounding proton ensemble ensures establishment of ^{15}N chemical shift vs. ^{15}N-^{1}H dipolar coupling correlation for virtually *all* amide ^{15}N-^{1}H spin-pairs in the sample independently on the orientation of the various peptide planes relative to the external magnetic field. Furthermore, the relatively large one-bond ^{15}N-^{1}H dipolar couplings ensure precise discrimination of differently oriented ^{15}N-^{1}H vectors within a relatively short t_1-evolution period causing a minimum of signal loss by $T_{1\rho}$ relaxation.

The alternative [$^{15}N_i$, $^{15}N_{i\pm1}$] chemical shift (2-b) and [^1H_i-$^{15}N_i$ dipolar coupling, $^{15}N_{i\pm1}$ chemical shift] (3-b) correlation experiments, providing similar resolution, require a time-consuming long-range $^{15}N_i \rightarrow {}^{15}N_{i\pm1}$ coherence transfer. Due to the low gyromagnetic ratio for ^{15}N, this transfer should preferentially be conducted via several intermediate (one-bond) coherence-transfer steps, each being susceptible to loss of signals due to coherence transfer via orientation-dependent dipolar couplings, or accomplished in a potentially less selective manner using homonuclear proton-driven ^{15}N spin-exchange (Szeverenyi et al., 1982). Both experiments may be implemented essentially as described by Marassi et al. (1999) in the context of oriented peptides, although we propose the additional use of pure exchange (PUREX) (deAzevedo et al., 2000) to suppress auto-correlations. This is fundamental to achieve the high resolution listed in Table 3. The pulse sequence using $t_1 = 0$ and $t_2 = 0$ to accomplish the 2-b and 3-b correlations, respectively, is shown in Figure 3b. We note that PUREX requires acquisition of two experiments with the second τ-delay placed either as shown in Figure 3b or moved to the position indicated by the curved arrow.

By combining the 2–3 and 2-b 2D experiments in a 2-3-b type 3D experiment (Marassi et al., 1999) correlating $^{15}N_i$ shift, ^1H_i-$^{15}N_i$ dipole coupling, and $^{15}N_{i\pm1}$ shift, it is possible to resolve 96% of the resonances in rhodopsin and 89% of the resonances in porin. This illustrates that this particular experiment is very attractive from the point of view of the highest possible resolution. One drawback of the present implementation, however, is the long mixing times of several seconds required to achieve efficient proton-

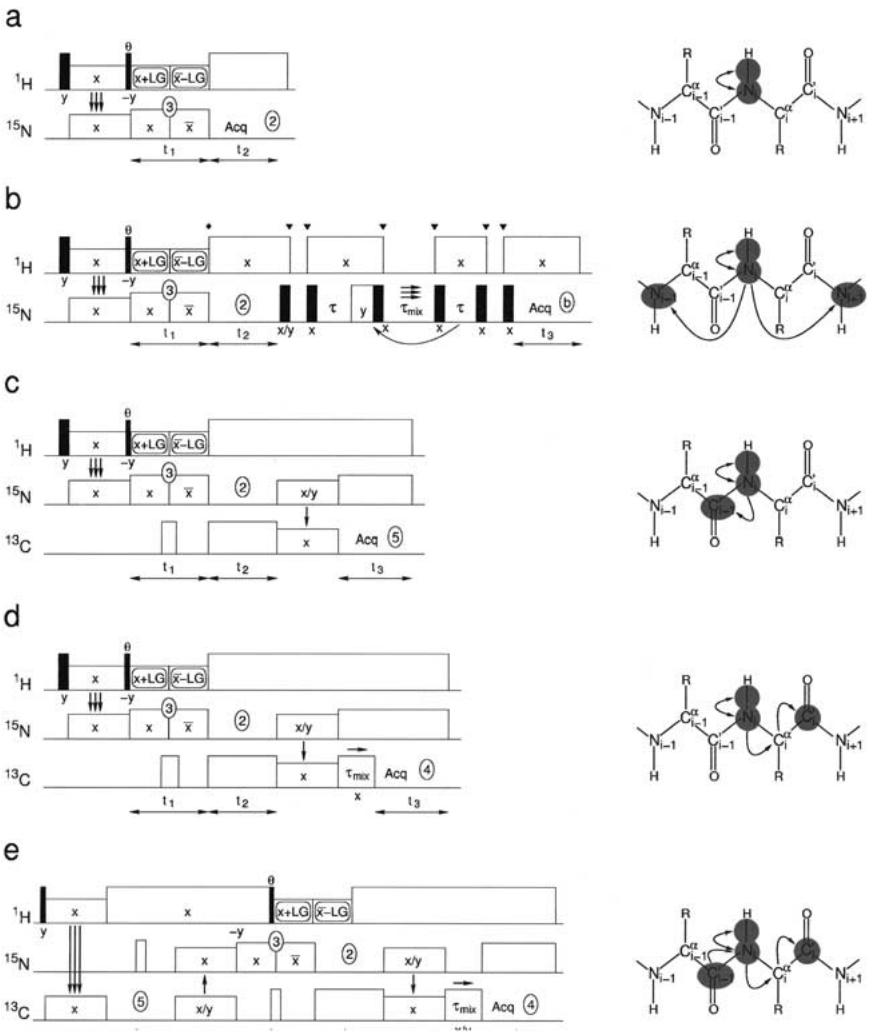

Figure 3. Pulse sequences proposed for (a,b) [^{1}H,^{15}N] double-resonance and (c–e) [^{1}H,^{13}C,^{15}N] triple-resonance experiments on macroscopically oriented membrane proteins. The experiments correlate the (a) ^{1}H-^{15}N dipole coupling with ^{15}N chemical shift (i.e., 2–3; implemented as PISEMA), (b) ^{1}H$_i$-^{15}N$_i$ dipole coupling with direct ^{15}N$_i$ and/or remote ^{15}N$_{i\pm1}$ chemical shift (2-3-b, 2-b, or 3-b), (c) ^{1}H$_i$-^{15}N$_i$ dipolar coupling with ^{15}N$_i$- and ^{13}C$'_{i-1}$ chemical shift (2-3-5), (d) ^{1}H$_i$-^{15}N$_i$ dipolar coupling with intra-residue ^{15}N$_i$- and ^{13}C$'_i$ chemical shifts established by transfer through the intermediate ^{13}C$^{\alpha}_i$ (2-3-4), and (e) ^{13}C$'_{i-1}$ chemical shift with ^{1}H$_i$-^{15}N$_i$ dipole coupling, ^{15}N$_i$ chemical shift, and ^{13}C$'_i$ chemical shift via ^{13}C$^{\alpha}_i$ (2-3-4-5). Non-selective and selective coherence transfers are indicated by triple and single arrows, respectively. If not indicated otherwise filled and open vertical bars are non-selective rf pulses with flip angles of $\pi/2$ and π, respectively. θ denotes a flip angle of $\pi/2 - \tan^{-1}\sqrt{2}$. The *x*/*y* phase combinations are used for phase-sensitive multiple-dimensional spectra according to States et al. (1982). Preferably, homonuclear decoupling should be applied during acquisition in (c–e) and also for the t_1 evolution period in (e). For the spin-diffusion experiment (b) the proton magnetization may be more efficiently utilized by placing ^{1}H *y*-phase $\pi/2$ and $\theta_{MA} = \tan^{-1}\sqrt{2}$ flip-back pulses at the positions indicated by black triangles and diamond, respectively. Thereby the relaxation delay and the first $\pi/2$ ^{1}H pulse may be omitted for all but the first scan. On the right are sketches of peptide sequences highlighting the relevant nuclei and transfer steps.

mediated spin-diffusion. This opens for uncontrolled leak of the magnetization to other spins potentially with the result of unwanted cross-peaks in the spectra which may lead to wrong assignments.

Addressing the alternative pure ^{13}C-labeling approach, although economically not the most obvious labeling strategy, it is interesting to note that the 2D ^{1}H-^{13}C$'$ chemical shift correlation experiments (1-4, 1-5, 1-c, a-4, and a-5) typically provide lower resolu-

tion than the best 2D ^{1}H-^{15}N counterparts. Adding the fact that all of these experiments additionally rely on time-consuming long-range coherence transfers, we will not discuss these further. In contrast, the selective 4-5 and non-selective 4-c 2D $^{13}C'$-$^{13}C'$ correlation experiments may prove useful since they simultaneously provide quite good resolution and useful correlations for sequential assignment.

Triple-resonance experiments

Realizing that it is difficult to establish sequential assignments from double-resonance experiments, we shall now use the results in Table 3 to evaluate which triple-resonance experiments yield the best resolution. Due to the above-mentioned problems with proton-mediated spin-diffusion, we focus on sequences employing selective (one-bond) transfer steps to 'walk' through the protein backbone. That is, the experiments should be carried out employing selective $^{13}C'_{i-1} \leftrightarrow {}^{15}N_i$, $^{15}N_i \leftrightarrow {}^{13}C^{\alpha}_i$, and $^{13}C^{\alpha}_i \leftrightarrow {}^{13}C'_i$ coherence transfers in a fashion similar to that extensively used in liquid-state NMR (for an overview see Cavanagh et al. (1996)) and more recently in MAS solid-state NMR of peptides (Straus et al., 1998; Hong, 1999; Pauli et al., 2001; Detken et al., 2001).

A liquid-state-inspired approach is to combine information from two experiments which establish correlation from the initial spin (e.g., $^{15}N_i$) to destination spins (e.g., $^{13}C'_{i-1}$ and $^{13}C'_i$) of the same type on the two sides within the peptide chain. Probably the most simple pair of experiments that provide sequential correlations is the 2D NCO and N(CA)CO experiments, which employ ^{15}N chemical shift evolution in the indirect dimension combined with observation of the $^{13}C'$chemical shift for the preceding (NCO) and same (N(CA)CO) residue as the initial amide nitrogen. In the latter experiment the magnetization is transferred to $^{13}C'_i$ via $^{13}C^{\alpha}_i$. By combining these two experiments the correlation between the $^{13}C'$ chemical shifts of adjacent residues may be achieved. Within our notation, the NCO and N(CA)CO experiments are labeled 2–5 and 2–4, respectively, which according to Table 3 provide resolution of 54–74% of the residues for rhodopsin and porin. While this may be a sufficient resolution to perform a complete assignment (Tycko, 1996), it is important to emphasize that the number of *correlations* established between two experiments is determined by the resolution in the dimension(s) the experiments have in common. For NCO and N(CA)CO, the common dimension is the ^{15}N chemical shift which provides only little resolution. Thus, employing the suggested two 2D experiments for our two model systems would only provide very few resolved pairs of sequential correlations although the resolution in both experiments is better than 50%.

The fact that only a very limited number of triad-spin sequential correlations (e.g., $^{13}C'_{i-1}$-$^{15}N_i$-$^{13}C'_i$) may be established from combination of 2D NMR experiments strongly suggests the use of three- or four-dimensional experiments for complete solid-state NMR assignment of ∼300 residue proteins. The most evident approach is to use NCO and N(CA)CO type of experiments in 3D versions employing evolution periods under the $^{1}H_i$-$^{15}N_i$ dipolar coupling, the $^{15}N_i$ chemical shift and the $^{13}C'_{i-1}$ or $^{13}C'_i$ chemical shift. The two relevant experiments are labeled 2-3-4 and 2-3-5 in Table 3 and allow resolution of 97–99% and 78–81%, respectively, of the signals in our model compounds.

The inter-residue 2-3-5 correlation experiment has already been implemented and experimentally demonstrated on oriented samples (Gu and Opella, 1999a, b; Ishii and Tycko, 2000), and relies on a PISEMA element followed by selective CP transfer from $^{15}N_i$ to $^{13}C'_{i-1}$], for the experiment with ^{13}C detection as sketched in Figure 3c. A major challenge in the ^{13}C-detected version of this experiment is to acquire the ^{13}C signal under homo- and heteronuclear decoupling as described by Ishii and Tycko (2000). The 2-3-4 experiment may be realized using the pulse sequence proposed in Figure 3d containing a PISEMA sequence, selective CP from $^{15}N_i$ to $^{13}C^{\alpha}_i$, and finally a homonuclear spin-lock period (see, e.g., Robyr et al., 1995) for transfer of coherence from $^{13}C^{\alpha}_i$ to $^{13}C'_i$. Apart from the expected gain in sensitivity by observation of higher-γ nuclei (Cavanagh et al., 1996), Table 1 indicates another advantage of ^{13}C detection, or to be more specific, a disadvantage of indirect ^{13}C detection. The reason is that the number of increments and thereby the time required for acquisition in an indirect dimension is inversely proportional to the required sampling rate. For ^{13}C the spectral window should accommodate both $^{13}C'$and side-chain ^{13}C spins to avoid folding of the latter into the carbonyl region of the spectrum. Consequently, the ^{13}C spectral window should cover a ∼250 ppm region provided the side-chain ^{13}C resonances can not be eliminated by other means. For ^{15}N detection the spectral window may be set to the span of the ^{15}N chemical shift tensor assuming that the number of ^{15}N resonances from other sources than the amide nitrogens are very few. Comparing the number of increments for indirect detection

of ^{13}C and ^{15}N chemical shifts listed in Table 1, we find that indirect ^{15}N detection typically requires only half the number of increments as required for indirect ^{13}C detection.

There is a remarkable difference in the number of resolved resonances for the 2-3-5 and 2-3-4 experiments, in favor of the novel inter-residue 2-3-4 experiment. Thus, it would be relevant to find alternative experiments to establish correlations to the $^{13}C'_{i-1}$ (5) spin. However, by consulting the results in Table 3, we realize that this dimension generally contributes little supplementary resolution to the $^{15}N_i$ chemical shift or $^{1}H_i$-$^{15}N_i$ dipolar coupling (*vide supra*). The most promising route to higher resolution in NCO-type experiments is to establish inter-residue correlations, i.e., experiments based on the [$^{13}C'_i$, $^{13}C'_{i-1}$ chemical shift correlation pulse sequence element labeled 4–5. When relying on one-bond transfers, this experiment may straightforwardly be extended to allow additional evolution periods under the $^{15}N_i$ chemical shift (the 3D experiment labeled 2-4-5) or the $^{1}H_i$-$^{15}N_i$ dipolar coupling (the 3D experiment labeled 3-4-5). Both approaches enable resolution of more than 95% of the resonances in our two model proteins, while the 4D 2-3-4-5 experiment resolves 99% of the resonances. Figure 3e proposes an implementation of this experiment starting with t_1 evolution under the $^{13}C'_{i-1}$ chemical shift followed by selective coherence transfer to $^{15}N_i$ for evolution under the $^{1}H_i$-$^{15}N_i$ dipolar coupling and ^{15}N chemical shift. Subsequently, the coherences are transferred to $^{13}C'_i$ via $^{13}C^{\alpha}_i$ by heteronuclear CP and homonuclear spin diffusion as described for the 2-3-4 experiment above. Obviously, a remaining question concerns whether it is experimentally realistic to perform these experiments involving three selective coherence transfer steps.

Topology-assisted spectral assignment

When discussing experimental techniques for assignment of solid-state NMR spectra for macroscopically oriented membrane proteins, it is not only relevant to address methods which establish sequential assignments through correlation of chemical shifts for the backbone (or side-chain) hetero nuclei. Much attention has recently been devoted to the use of the so-called polarization index slant angle (PISA) wheels for topology-based interpretation of PISEMA type [^{1}H,^{15}N]-double-resonance spectra of oriented uniformly ^{15}N-labeled peptides (Marassi and Opella, 2000; Wang et al., 2000; Marassi, 2001). By exploiting the characteristic orientation of the ^{15}N chemical shift and ^{1}H-^{15}N dipolar coupling tensors relative to the peptide plane (cf. Figure 1) in a well-defined secondary structure, it has proven possible to assign PISEMA spectra for small peptides sequentially without the need for dipolar- or J-coupling-mediated coherence transfers between residues. Furthermore, the location and shape of the PISA wheels (i.e., wheel-like patterns in the 2D spectra on which the resonances from a well-defined secondary structure are located) will under ideal conditions allow direct assessment of the rotational pitch and tilt angle defining the average molecular axis relative to the magnetic field.

With the focus of this paper being virtually all kinds of multi-dimensional correlations experiments involving chemical shift and dipolar coupling interactions of most nuclei associated with the peptide planes, it is appropriate to demonstrate that PISA wheels are by no means restricted to correlations between the ^{1}H chemical shift, ^{15}N chemical shift, and the ^{1}H-^{15}N dipolar coupling in uniformly ^{15}N-labeled peptides. Any correlation between peptide-plane-fixed interactions will lead to PISA-wheel like structures (in two or more dimensions), which may be taken into advantage for assignment and structure determination. To illustrate this feature and the diversity in the 'geometric' appearances, Figure 4 contains representative wheels which may be observed in [$^{15}N_i$, $^{15}N_{i\pm1}$] (2-b), [$^{15}N_i$, $^{13}C'_{i-1}$ (2–5), and [$^{15}N_i$, $^{13}C'_i$ (2–4) chemical-shift correlation experiments for ideal α-helical and β-sheet structures with different orientation of the molecular axis relative to the external field. The wheels are obtained by mapping contributions from molecules with rotational pitches (i.e., rotations around the molecular axis) between 0 and 2π. From these plots it is quite evident that different correlation experiments produce widely different patterns depending on the peptide tilt angle and secondary structure, which, in addition to assignment information, may be taken into advantage as a probe to accurate information about the structure and membrane-associated topology of the peptide.

For large proteins, PISA-wheel like patterns in multiple-dimensional correlation experiments may also be used for assignment and structure determination purposes, e.g., by computer-assisted spectral interpretation. It is important to note, however, that several factors may complicate the direct use of such procedures. First, it is clear that the resolution issues discussed above also apply for the identification of wheel structures, implying that the best compromise between resolution power and secondary structure/topology definition should be found. Second, the

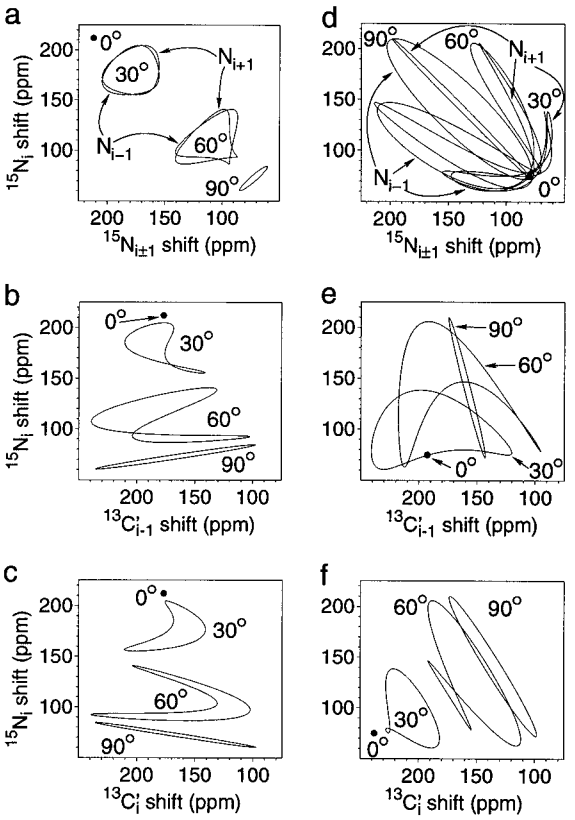

Figure 4. SIMMOL simulated two-dimensional PISA wheels for ideal (a–c) α-helix ($\phi = -65°$, $\psi = -40°$) and (d–f) β-sheet ($\phi = -135°$, $\psi = 140°$) structures with tilt angles of 0°, 30°, 60°, and 90° relative to the magnetic field direction. The spectra represent (a,d) the 2-b experiment overlaying [N_i, N_{i-1}] and [N_i, N_{i+1}] wheels, (b,e) the 2-5 experiment, and (c,f) the 2–4 experiment with the involved interactions more clearly specified along the axes.

identification of wheels may in practice be complicated by variation of the torsion angles around the typical secondary-structure values (e.g., induced by kinked or bent structures) which leads to fluctuations of the resonances around the predicted wheels (Wang et al., 2000; Bak et al., 2001a, 2002). Third, less defined structure elements such as inter-helical extra-membrane loops may accidentally contribute signals in spectral regions where they can not easily be distinguished from PISA-wheel contributing resonances from well-defined structure elements. Fourth, the resonance positions, and thereby the definition of the wheel, may depend on the experimental procedure as well as the available/desirable rf field strengths, rf homogeneity etc., being important for suppression of complicating effects from undesired nuclear spin interactions (Bak et al., 2002). Overall these factors may severely complicate exclusive use of PISA-wheel type spectral patterns for assignment and structure determination for large membrane proteins. However, it should be emphasized that these patterns may still prove very valuable in combination with other techniques providing supplementary assignment and structure information.

Sensitivity

Considering that for non-rotating solids, the dipole-dipole coupling interaction will typically be the preferred coherence-transfer medium, it is important to realize that the oriented-sample approach most likely will be associated with considerable variations in signal intensity depending on the actual orientation of the internuclear vectors relative to the external magnetic field. For example, if an internuclear vector forms the magic angle ($\tan^{-1}\sqrt{2}$) with the external field, the effective dipolar coupling vanishes implying that there will be no direct dipolar-coupling-mediated coherence transfer between these two nuclei. To substantiate this problem, Figure 5 shows the distribution in sizes of various relevant effective one-bond dipolar couplings in an ideal α-helix exhibiting different tilt angles relative to the external magnetic field (Figures 5a–d) and for rhodopsin with the average helical axis oriented co-linear with the magnetic field (Figures 5f–h). In this context, we define the effective dipolar coupling as $(b_{IS}/2\pi)(3\cos^2\beta_{PL} - 1)/2$, where $b_{IS} = -\gamma_I\gamma_S\mu_0\hbar/(r_{IS}^3 4\pi)$ is the dipolar coupling constant (in angular frequency units) with γ_I, γ_S being the gyromagnetic ratios of the two nuclei and r_{IS} the distance between these, while β_{PL} is the angle between the internuclear vector and the magnetic field. From the plots in Figure 5 it is evident that even quite small tilts of the helical axis away from a pure trans-membrane orientation will cause a substantial variation in the effective dipolar couplings needed for selective coherence transfer. Furthermore, a largely uniform distribution of effective dipolar couplings may be very typical for large membrane proteins considering that (*i*) they in addition to membrane spanning regions typically will contain large extra-membrane parts with less well-defined structure and (*ii*) trans-membrane helices in bundles very often have non-zero tilt angles, often are kinked (e.g., in the presence of proline residues), and typically will have non-vanishing helix crossing angles (Bowie, 1997; Unger et al., 1997; Bywater et al., 2001; Teller et al., 2001; Bak et al., 2001b). Indeed, most of this applies for rhodopsin as clearly manifested by the effective dipolar coupling distribution bars in Figures 5e and 5f, where the

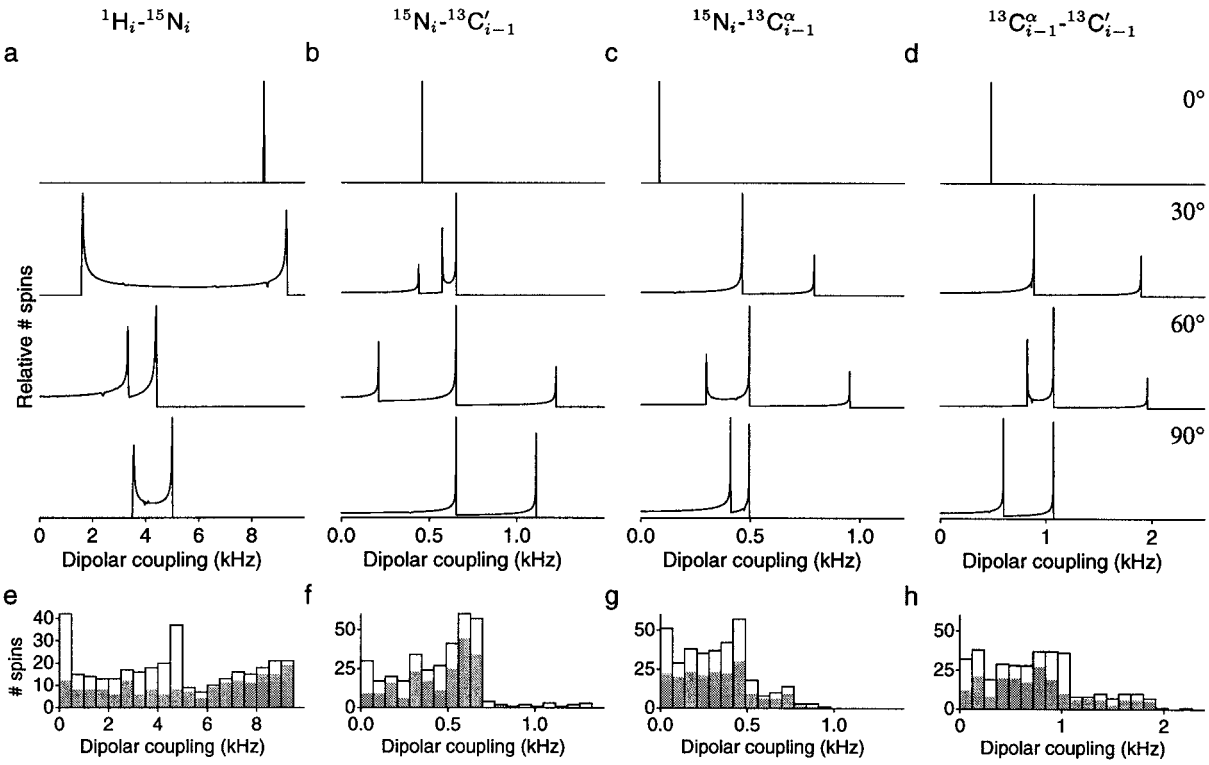

Figure 5. Distributions (relative and absolute number of spins) of the (a,e) $^{1}H_i$-$^{15}N_i$, (b,f) $^{15}N_i$-$^{13}C'_{i-1}$, (c,g) $^{15}N_i$-$^{13}C^{\alpha}_{i}$, and (d,h) $^{13}C^{\alpha}_{i}$-$^{13}C'_{i}$ effective dipolar couplings determined using SIMMOL (see definition in text) in (a-d) an ideal α-helix tilted 0°, 30°, 60°or 90° relative to the external magnetic field (averaging over all rotational pitches from 0 to 2π), and (e–h) for rhodopsin with the average helix axis oriented parallel to the static field. The shaded bars in (e–h) designate the distributions of the effective dipole couplings from the seven TM helices in rhodopsin alone.

shaded parts reflect contributions from the seven transmembrane helices alone, for which a much smaller variation in effective dipolar couplings intuitively may have been anticipated.

With the ultimate goal being both excitation and resolution of all resonances, it appears fundamental to investigate the excitation profiles of the various pulse-sequence elements constituting the building blocks of resolution-wise attractive multiple-dimensional pulse sequences. In this evaluation it is relevant to distinguish between selective and non-selective transfers. According to the effective dipolar coupling distributions described above, selective transfers will be susceptible to orientation-dependent signal loss, while the non-selective pulse sequences typically will excite all coherences but may cause distribution of these to undesired nuclei with the consequences of sensitivity-loss and ambiguous correlations. The latter disadvantage will obviously only occur if the pulse sequence element separates evolution periods corresponding to different frequency dimensions of the multiple-dimensional experiment.

The PISEMA experiment is initialized by a *non-selective* ^{1}H to ^{15}N cross-polarization (CP) coherence transfer, which in principle allows excitation of resonances from all amide ^{15}N nuclei independently on the orientation of the involved peptide plane. To illustrate this very attractive feature numerically, we have calculated the intensities of a PISEMA spectrum for 18 residues in an ideal poly-alanine α-helix exhibiting different helix tilt angles relative to the external field. The ensemble of protons surrounding the amide ^{15}N nucleus is represented by the six closest protons, all with ^{1}H-^{15}N dipolar couplings larger than 500 Hz, i.e., the relevant spin system includes $^{15}N_i$, $^{1}H_i$, $^{1}H^{\alpha}_{i}$, $^{1}H_{i+1}$, $2 \times {}^{1}H^{\beta}_{i}$, and $1 \times {}^{1}H^{\beta}_{i-1}$. Employing this spin system in a SIMPSON simulation of the $^{1}H \rightarrow {}^{15}N$ CP coherence-transfer efficiency of the PISEMA experiment, we find that the sensitivity is largely independent on the overall orientation of the peptide

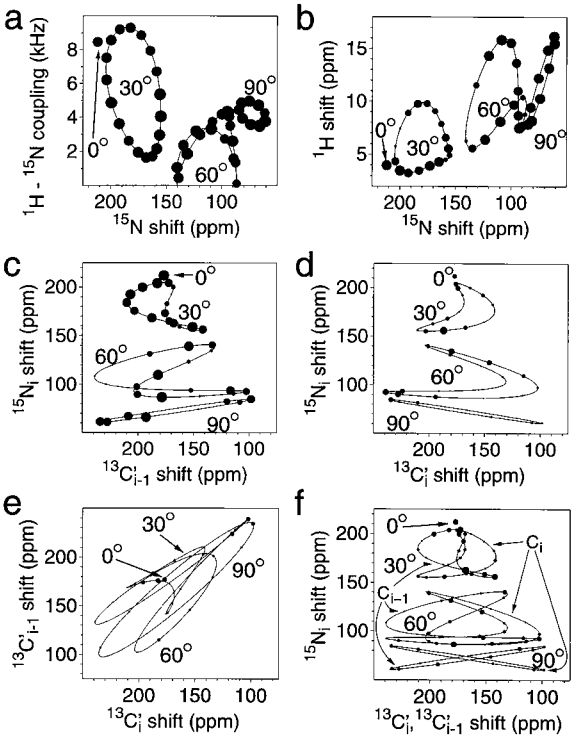

Figure 6. SIMPSON/SIMMOL simulated PISA wheels illustrating the orientation dependence on the transfer efficiencies for different one-bond coherence transfer routes in an ideal 18-residue α-helix ($\phi = -65°$, $\psi = -40°$) oriented with different tilt angles with respect to the magnetic field. The solid lines represent the theoretical PISA wheels corresponding to the indicated tilt angle while the filled circles designate specific resonance positions for the 18 residues with the circle diameter being proportional to the transfer efficiency (cf. Table 4). The six spectra demonstrate PISA wheels correlating (a) intra-residue ^{1}H$_i$-^{15}N$_i$ dipolar coupling vs. ^{15}N$_i$ chemical shift (2-3, or the PISEMA experiment (Wu et al., 1994) in Figure 1a), (b) intra-residue ^{1}H$_i$ vs. ^{15}N$_i$ chemical shift (1–2) (Marassi, 2001), (c) inter-residue ^{15}N$_i$ vs. ^{13}C$'_{i-1}$ chemical shift (2–5), (d) intra-residue ^{15}N$_i$ vs. ^{13}C$'_i$ chemical shift (2–4), (e) inter-residue ^{13}C$'_{i-1}$ vs. ^{13}C$'_i$ chemical shift (4–5), and (f) intra- and inter-residue ^{15}N$_i$ vs. ^{13}C$'_i$ and ^{13}C$'_{i-1}$ chemical shift (2-4,5). All correlations use were established by CP-type mixing sequences using the optimized parameters in Table 4 (vide infra).

as well as the local orientation of the peptide planes. This is illustrated in Figure 6a, where the solid lines represent the PISA wheel shape (Marassi and Opella, 2000; Wang et al., 2000) for the indicated helix tilt angles and the filled circles correspond to the resonances for the 18 residues in our ideal helix. The diameter of the filled circles is proportional to the coherence-transfer amplitude, in this case being largely identical for all residues.

The closely related ^{1}H vs. ^{15}N chemical shift correlation experiment, although being far less attractive from a resolution point-of-view, relies on *selective* ^{1}H$_i \rightarrow {}^{15}$N$_i$ CP coherence transfer and will therefore exhibit different sensitivity for differently oriented residues. This feature becomes clearly evident from Figure 6b showing ^{1}H vs. ^{15}N chemical shift PISA wheels (Marassi, 2001) of an ideal α-helix exhibiting different tilt angles relative to the external field and with the diameter of the filled resonances being proportional to the selective ^{1}H$_i \rightarrow {}^{15}$N$_i$ CP coherence-transfer amplitude. Although the sensitivity is generally good, we note that the resonances from certain residues in helices with tilt angles of 30° and 60° have almost disappeared from the spectrum due to unfortunate orientations of the ^{1}H-^{15}N internuclear vectors. Obviously, such losses (which depend both on the helix tilt and the rotational pitch) may complicate the use of the spectrum for assignment or structure determination unless used in combination with other experiments providing complementary information for the non-excited nuclei.

The three one-bond coherence transfers that are of particular interest as building blocks in the triple-resonance experiments discussed above, namely ^{15}N$_i \rightarrow {}^{13}$C$'_{i-1}$, ^{15}N$_i \rightarrow {}^{13}$C$^{\alpha}_i$, and ^{13}C$^{\alpha}_i \rightarrow {}^{13}C'_i$, are challenging to implement for two reasons. First, they are based on selective coherence transfer through effective dipolar couplings which according to Figure 5 display similar fluctuations as the ^{1}H-^{15}N dipolar couplings. Thus, these transfers will most likely be associated with similar orientation-dependent coherence-transfer efficiencies as observed above for the ^{1}H vs. ^{15}N chemical shift correlation experiment. Second, the competing, but undesired, two-bond coherence transfers (e.g., the N$_i \rightarrow {}^{13}$C$'_i$ transfer in the case of the desired one-bond N$_i \rightarrow {}^{13}$C$'_{i-1}$ transfer) need to be suppressed as efficiently as possible to reduce sensitivity loss and, in particular, to prevent the presence of two-bond cross-peaks in the spectra which may lead to ambiguities in the spectral assignment.

To investigate these aspects and propose optimal solutions in terms of practically relevant pulse sequences, we used SIMPSON to numerically evaluate the efficiencies of desired and undesired coherence transfer processes for traditional Hartman–Hahn type CP experiments on representative four-spin systems within an ideal α-helix oriented with different tilt angles and for rhodopsin uniaxially oriented with the average helix axis along the external magnetic field. Specifically, the calculations employed the (^{13}C$'_{i-1}$, ^{15}N$_i$, ^{13}C$^{\alpha}_i$, ^{13}C$'_i$) spin-system for the ^{15}N$_i \rightarrow {}^{13}$C$'_{i-1}$

Table 4. Numerically optimized pulse-sequence parameters[a] for heteronuclear $^{15}N \rightarrow {}^{13}C$ cross-polarization and homonuclear $^{13}C^{\alpha} \rightarrow {}^{13}C'$ coherence transfer by rf driven spin diffusion for ideal 18-residue α-helices ($\phi = -65°$, $\psi = -40°$) with different tilt angles and for rhodopsin oriented with the average helical axis along the external magnetic field

System	τ_p (μs)	ν_{rf}^{N} (kHz)	ν_{rf}^{C} (kHz)	$\nu_{carrier}^{N}$ (ppm)	$\nu_{carrier}^{C}$ (ppm)	Efficiency		Loss[c]
						Desired (%)	Undesired[b] (%)	(%)
$^{15}N_i \rightarrow {}^{13}C'_{i-1}$ transfer (2-5):								
Helix, 0°	1037	37.0	37.0	186	188	93	2	0
Helix, 30°	862	37.0	37.0	109	160	61	2	11
Helix, 60°	605	37.1	36.9	201	163	44	2	22
Helix, 90°	590	37.3	36.9	145	168	54	1	22
Rhodopsin	825	40.1	39.9	130	160	58	3	11
$^{15}N_i \rightarrow {}^{13}C_i^{\alpha}$ transfer:								
Helix, 0°	4000	9.3	9.3	161	22	65	1	0
Helix, 30°	937	8.9	8.9	205	31	62	3	11
Helix, 60°	1009	8.9	8.9	218	29	62	2	11
Helix, 90°	1226	8.2	8.2	225	26	60	8	22
Rhodopsin	1014	16.8	16.9	152	32	50	4	16
$^{13}C_i^{\alpha} \rightarrow {}^{13}C'_i$ transfer:								
Helix, 0°	2264	29.0	–	–	79	53	1	0
Helix, 30°	697	50.0	–	–	111	37	1	22
Helix, 60°	593	50.0	–	–	121	33	2	22
Helix, 90°	999	45.0	–	–	124	22	4	11
Rhodopsin	773	50.0	–	–	105	33	2	23
$^{15}N_i (\rightarrow {}^{13}C_i^{\alpha}) \rightarrow {}^{13}C'_i$ transfer (2–4):								
Helix, 0°	–	–	–	–	–	35	1	0
Helix, 30°	–	–	–	–	–	19	1	22
Helix, 60°	–	–	–	–	–	21	1	28
Helix, 90°	–	–	–	–	–	12	3	33
Rhodopsin	–	–	–	–	–	14	3	32
$^{15}N_i \rightarrow {}^{13}C'_i$ direct transfer (2–4):								
Helix, 0°	4000	20.0	20.0	178	91	43	4	0
Helix, 30°	2589	47.0	47.0	93	102	16	24	0
Helix, 60°	3618	41.0	41.0	56	140	15	19	6
Helix, 90°	3725	42.4	42.3	34	126	13	18	11
Rhodopsin	2641	49.9	49.6	154	101	11	25	15
$^{13}C'_{i-1} (\rightarrow {}^{15}N_i \rightarrow {}^{13}C_i^{\alpha}) \rightarrow {}^{13}C'_i$ transfer (2–5):								
Helix, 0°	–	–	–	–	–	33	–	0
Helix, 30°	–	–	–	–	–	9	–	28
Helix, 60°	–	–	–	–	–	9	–	22
Helix, 90°	–	–	–	–	–	8	–	33
Rhodopsin	–	–	–	–	–	8	–	41

[a]The parameters include the Hartman–Hahn contact time (spin-lock period) τ_p, the ^{13}C and ^{15}N rf field strengths ν_{rf}^{C} and ν_{rf}^{N}, and the two corresponding rf carrier frequencies $\nu_{carrier}^{C}$ and $\nu_{carrier}^{N}$. All simulations correspond to a ^{1}H Larmor frequency of 400 MHz.

[b]The undesired spin is the spin of same type as the desired target spin, but separated from the initial spin by two bonds.

[c]Percentage of signals which are less intense than 20% of the average peak intensity.

transfer, ($^{13}C^{\alpha}_{i-1}$, $^{13}C'_{i-1}$, $^{15}N_i$, $^{13}C^{\alpha}_i$) for the $^{15}N_i \rightarrow {}^{13}C^{\alpha}_i$ transfer, and ($^{13}C'_{i-1}$, $^{13}C^{\alpha}_i$, $^{13}C^{\beta}_i$, $^{13}C'_i$) for the $^{13}C^{\alpha}_i \rightarrow {}^{13}C'_i$ transfer. Using this setup, relevant SIMMOL-established tensor orientations, and SIMPSON in a new combination with the iterative minimization tools of MINUIT (James and Ross, 1975), we conducted a numerical iterative search for experimental conditions at 9.4 T giving the best average coherence transfer to the desired spins while suppressing transfers to the various undesired spins. This was accomplished using appropriate combinations of grid scan, Monte Carlo, Simplex, and steepest-descend procedures to systematically search for the maximum absolute value of the intensity function $\sum I(X) - I(X') - I(Y)$, where X denotes the desired target spin, X and Y the undesired destination spins, and where the summation includes all residues. The rf carrier frequencies, the rf field strengths, and the CP contact time are the free variables in the optimization. To restrict the investigations to the experimentally most realistic conditions, the CP contact time and rf field strengths were not allowed to exceed 4 ms and 50 kHz, respectively.

Table 4 summarizes the results of these pulse-sequence building-block optimizations by showing the optimum pulse-sequence parameters and the overall transfer efficiency to the desired (and undesired) target spins. For all of the selected one-step, one- or two-bond, transfers we observe that the average transfer efficiencies are significantly lower than 100%. This is not surprising considering that it is difficult to establish optimum selective CP transfer conditions for samples with a large distribution of effective dipolar couplings as reflected in Figure 5. Another trend is that in all cases it has been possible to suppress the average of the competing, and highly undesired, two-bond transfers to less than 8% of the average intensity on the desired spin. Furthermore, Table 4 provides information about the potential loss of signals (as already addressed by the intensity distributions for the PISA wheels in Figure 6) expressed as the fraction of the signals that is excited with less than 20% of the average intensity transferred to the desired spin. We note that in practice, the signal-to-noise ratio will often be sufficient to clearly observe resonances with substantially lower intensity than this quite conservative threshold. Lowering the threshold value will obviously reduce the number of lost correlations.

Intuitively we expect that not all parameters have the same impact on the coherence transfer amplitudes.

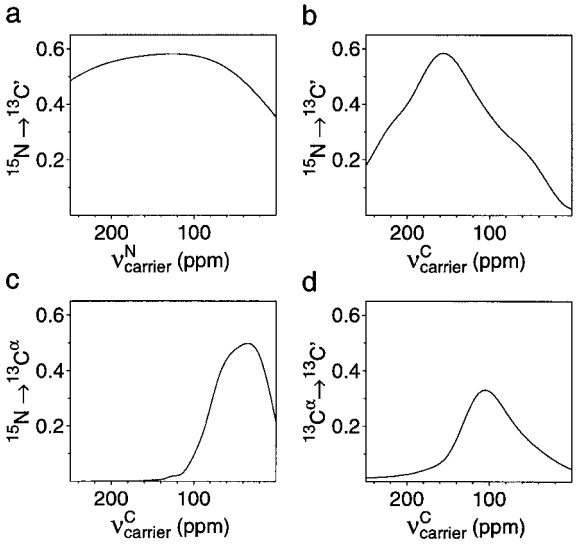

Figure 7. Average coherence transfer efficiencies for (a,b) the $^{15}N \rightarrow {}^{13}C'$, (c) $^{15}N \rightarrow {}^{13}C^{\alpha}$, and (d) $^{13}C^{\alpha} \rightarrow {}^{13}C'$ coherence transfer as function of the ^{15} N (a) and ^{13}C (b–d) rf carrier frequencies.

For example, the ^{13}C carrier frequency may play a fundamental role in distinguishing between $^{15}N \rightarrow {}^{13}C'$ and $^{15}N \rightarrow {}^{13}C^{\alpha}$ transfer. Indeed, Table 4 reveals that the ^{13}C transmitter should be placed in the carbonyl chemical-shift range about 160–180 ppm for optimum $^{15}N \rightarrow {}^{13}C'$ transfer while it should be placed in the aliphatic region about 20–30 ppm for optimum $^{15}N \rightarrow {}^{13}C^{\alpha}$ transfer. Likewise, the carrier should be placed in-between the $^{13}C'$ and $^{13}C^{\alpha}$ resonance frequencies for efficient transfer between these spin species. In contrast, we observe large fluctuations in the ^{15}N transmitter carrier frequency for heteronuclear transfers depending on the actual molecular orientation. To investigate the significance of these parameters, Figure 7 shows the average coherence transfer amplitudes for rhodopsin for the different CP coherence transfers as function of the ^{15}N and ^{13}C rf carrier frequencies. It is immediately evident that the transfer efficiency is only marginally influenced by the ^{15}N carrier frequency within the frequency range of the amide ^{15}N chemical shift anisotropy (Figure 7a) as also reflected by the large and apparently random scattering of this parameter in Table 4. In contrast, both homo- and heteronuclear transfers are significantly influenced by the ^{13}C carrier frequency as illustrated in Figures 7b–d. This emphasizes the need for careful adjustment of this parameter, but also demonstrates its control capacity for accomplishing the desired selective coherence transfers.

The heteronuclear $^{15}N_i \rightarrow {}^{13}C'_{i-1}$ coherence transfer, involved in 2–5 type experiments, provides a quite favorable sensitivity in the sense that an average of 58% of the initial coherence for rhodopsin is transferred to the desired target spin, while keeping the fraction of resonances excited with less than 20% of the average signal intensity as low as 11%. This is qualitatively in good agreement with the impression already obtained from simulation of [$^{15}N_i$, $^{13}C'_{i-1}$] PISA wheels for differently oriented α-helices in Figure 6c. A less favorable example is the $^{13}C_i^{\alpha} \rightarrow {}^{13}C'_i$ transfer, being the second step in the one-bond transfer-based two-bond $^{15}N_i \rightarrow {}^{13}C'_i$ (i.e., 2–4) coherence transfer. In this case the optimum average transfer efficiency is not higher than 33% for rhodopsin, while the potential for loss of signals increases to 23%. The relatively low transfer efficiency may be ascribed to the fact that a significant fraction of the initial coherences is lost by simultaneous one-bond transfer to $^{13}C_i^{\beta}$. For rhodopsin the average intensity lost on the $^{13}C^{\beta}$ spins amounts to 15% of the total intensity. While the appearance of $^{13}C^{\beta}$ signals will not disturb in the carbonyl region of the ^{13}C spectrum, the low transfer amplitudes are not too promising for the two-step $^{15}N_i$ ($\rightarrow {}^{13}C_i^{\alpha}$) $\rightarrow {}^{13}C'_i$ (2–4) coherence transfer. Indeed, Table 4 reveals that the overall amplitude for this independently optimized two-step transfer averages to 14% for rhodopsin using the optimum pulse sequence parameters listed for the individual one-bond transfers.

Considering that about 85% of the coherences are lost by combining two highly orientation-dependent and leaking one-bond coherence transfers, it is tempting to consider whether the less selective *direct* two-bond $^{15}N_i \rightarrow {}^{13}C'_i$ (2-4) coherence transfer as proposed by Ishii and Tycko (2000) would be a reasonable alternative upon appropriate optimization of the involved rf field strengths, rf carrier frequencies, and CP contact time. In this regard, Table 4 demonstrates that the direct transfer is largely associated with the same transfer efficiency as the combined two-step approach. It is important, however, to realize that the direct two-bond experiment may suffer from additional serious drawbacks. First, considering that the effective two-bond $^{15}N_i$-$^{13}C'_i$ dipolar couplings on the average are five times weaker than the corresponding one-bond $^{15}N_i$-$^{13}C'_{i-1}$ dipolar couplings, it is difficult to optimize the experiment to avoid significant signal contributions from the competing $^{15}N_i \rightarrow {}^{13}C'_{i-1}$ transfer as evidenced in Table 4 by typical transfer efficiencies on the order of 15% to both $^{13}C'_i$ and $^{13}C'_{i-1}$ even when using pulse sequence parameters optimized for the two-bond transfer. This drawback also becomes evident from the PISA wheels in Figure 6f which apart from different transfer efficiencies (as represented by the diameter of the filled resonance circles) combines the two 2–5 and 2–4 wheels from Figures 6c and 6d, respectively. Second, the fact that the spectrum represent a super position of 2–4 and 2–5 wheels which complicates unambiguous assignment and reduces the overall resolution of the experiment significantly relative to the desired 2–4 experiment. Explicitly, the 2-(4,5) experiment resolves only 44% and 54% of the resonances for rhodopsin and porin, respectively, as compared to the 73% and 74% offered by the more selective 2-4 experiment. A similar trend is observed for the 3-(4,5) and 2-3-(4,5) experiments allowing resolution of 38%/46% and 77%/79% of the resonances for rhodopsin/porin. Third, due to the relatively small effective dipolar couplings the time required for efficient two-bond transfer is generally somewhat higher than the time required for the relevant two one-bond transfers, implying that the former experiment generally will display additional sensitivity losses due to relaxation. Overall, this suggests the use of the two-step experiment using a pulse sequence of the type shown in Figure 3d rather than the less specific two-bond experiment.

Facing the quite large distributions of effective dipolar couplings generally present for oriented samples (cf. Figure 5), any pulse sequence relying on selective dipolar-coupling-mediated coherence transfer will typically display a relatively large variation in the signal intensities as evident from Table 4 and Figure 6. An important exception, however, is experiments using initial transfer from an ensemble of spins, as exemplified by the PISEMA spectrum (cf. Figure 6a). For the more typical selective transfers, where low sensitivity and in particular loss of signals may be problematic, we suggest either the combination of complementary experiments with different orientation dependency or the design of techniques with reduced orientational dependency. The latter may include broadband pulse sequences based on composite dipolar coupling evolution periods as recently described for heteronuclear couplings in the context of weakly aligned molecules in solution (Schulte-Herbrüggen et al., 2001) or pulse sequences based on coherence transfer mediated by isotropic J-coupling as discussed extensively in the context of rotating powder samples (Baldus and Meier, 1996; Detken et

al., 2001). Furthermore, for the homonuclear $^{13}C^{\alpha} \rightarrow {}^{13}C'$ rf-mediated transfer we have observed, from optimizations allowing the rf field strength to exceed 50 kHz, that higher field strengths provide better transfer. Overall this may suggest the use of isotropic-mixing sequences (Shaka et al., 1983; Robyr et al., 1995) with better compensation for chemical-shift differences between the initial and target spins at experimentally convenient rf-field strengths.

Conclusions

In conclusion, we have applied state-of-the-art software for numerical simulation of solid-state NMR spectra for uniaxially oriented and uniformly ^{15}N or [^{13}C,^{15}N]-isotope labeled membrane proteins in the 30–40 kDa regime. Using appropriate combinations of SIMMOL and SIMPSON calculations with typical isotropic and anisotropic nuclear spin interactions, we have systematically analysed all one- to six dimensional experiments correlating ^{1}H amide, ^{15}N amide, $^{13}C'$ chemical shifts and ^{1}H-^{15}N dipolar couplings in model peptides as well as rhodopsin and porin representing typical α-helical and β-barrel membrane protein structures.

At least three aspects prove very important in the search for optimum experimental procedures: (i) the overall resolution power of the experiment, (ii) the ability to produce sequential assignments, and (iii) the orientation-dependent excitation profiles for the correlation experiments. In practice these qualities, obviously, need to be considered along with the available isotope-labeling patterns and the available instrumentation (e.g., double- or triple-resonance equipment).

Focusing on [^{1}H,^{15}N] double-resonance experiments, the already well-established PISEMA experiment offers resolution of about 50–60% of the resonances for rhodopsin and porin with largely uniform excitation of all resonances. Since this experiment exclusively establishes intra-residue assignments and information about the orientation of the individual peptide planes relative to the external magnetic field, sequential assignments need to be established as information from so-called PISA wheel patterns being difficult for large uniformly ^{15}N labeled proteins. Alternatively, and more rigorously, sequential assignments may be obtained using an intra-residue [$^{15}N_i$, $^{15}N_{i\pm1}$] correlation experiment providing similar resolution power as PISEMA. Combination of these two 2D experiments into a 3D experiment ideally improves the resolution to about 90–95% of the resonances, although it appears relevant to note that it practically may be difficult to establish the long-range ^{15}N-^{15}N coherence transfers without leak to undesired spins reducing the sensitivity, resolution, and complicating assignments.

Allowing for additional ^{13}C labeling, a variety of two- and three-dimensional experiments, among which the 3D combinations of PISEMA with frequency labeling by the $^{13}C'_i$ or $^{13}C'_{i-1}$ chemical shifts are particularly attractive. The former (intra-residue) experiment proposed in this work resolves 97–99% of the resonances for rhodopsin and porin, while the earlier proposed inter-residue experiment (Gu and Opella, 1999a) resolves about 80% of the resonances. The 4D experiment combining these two 3D experiment resolves 99% of the resonances while the 3D [$^{15}N_i$, $^{13}C'_i$, $^{13}C_{i-1}$] chemical shift correlation experiment resolves 95% of the resonances. In general these experiments are based on selective coherence transfers, which according to the SIMMOL analysis presented in this paper, cause structure/orientation dependent signal intensities in the correlation experiments. To cope optimally with this situation we have used SIMMOL in combination with SIMPSON to numerically optimize pulse sequence parameters for optimum performance in the most typical α-helical type of large membrane proteins.

With these and several other examples presented in this paper, it should be demonstrated that the macroscopically oriented sample approach for solid-state NMR studies of membrane proteins by appropriate choice of experimental methods should be capable of providing full backbone assignment and structure determination for proteins significantly larger than than those studied so far. Furthermore, it should be evident that SIMMOL in combination with SIMPSON provides an efficient tool for numerical simulation, evaluation, and optimization of experimental solid-state NMR methods for macroscopically oriented membrane proteins. The analyses are sufficiently simple that they may readily be repeated for any kind of protein for which atomic coordinates are available. With the two most typical membrane-protein structural motifs covered, we demonstrated the utility of this approach and envisage that many useful guidelines as to the design and application of experimental methods should be directly available from the present analysis.

Acknowledgements

This research was supported by grants from The Danish Research Agency in relation to the Danish Biotechnology Instrument Center (J. No. 0002214), Carlsbergfondet (J. No. 990258), and Novo Nordisk Fonden.

References

Appleyard, A.N., Herbert, R.B., Henderson, P.J.F., Watts, A. and Spooner, P.J.R. (2000) *Biochim. Biophys. Acta*, **1509**, 55–64.

Arkin, I.T., Brünger, A.T. and Engelman, D.M. (1998) *Proteins*, **28**, 465–466.

Bak, M., Rasmussen, J.T. and Nielsen, N.C. (2000) *J. Magn. Reson.*, **147**, 296–330. Internet address: http://nmr.imsb.au.dk

Bak, M., Schultz, R. and Nielsen, N.C. (2001a) In *Perspectives on Solid State NMR in Biology*, Kiihne, S.R. and de Groot, H.J.M. (Eds.), Kluwer Academic Publishers, Dordrecht, pp. 95–109.

Bak, M., Bywater, R.P., Hohwy, M., Thomsen, J.K., Adelhorst, K., Jakobsen, H.J., Sørensen, O.W. and Nielsen, N.C. (2001b) *Biophys. J.*, **81**, 1684–1698.

Bak, M., Schultz, R., Vosegaard, T. and Nielsen, N.C. (2002) *J. Magn. Reson.*, **154**, 28–45. Internet address: http://nmr.imsb.au.dk

Baldus, M. and Meier, B.H. (1996) *J. Magn. Reson.*, **A121**, 65–69.

Bernstein, F.C., Koetzle, T.F., Williams, G.J.B., Meier Jr., E.F., Brice, M.D., Rodgers, J.R., Kennard, O., Shimanouchi, T. and Tasumi, M. (1977) *J. Mol. Biol.*, **112**, 535–542. Internet address: http://www.rcsb.org/pdb

Bowie, J.U. (1997) *J. Mol. Biol.*, **272**, 627–636.

Bywater, R.P., Thomas, D. and Vriend, G. (2001) *J. Comput. Aided Mol. Des.*, **15**, 533–552.

Cavanagh, J., Fairbrother, W.J., Parmer III, A.G. and Skelton, N.J. (1996) *Protein NMR Spectroscopy: Principles and Practice*, Academic Press, San Diego, CA.

Cornilescu, G., Delaglio, F. and Bax, A. (1999) *J. Biomol. NMR*, **13**, 289–302.

Cross, T.A. and Quine, J.R. (2000) *Concepts Magn. Reson.*, **12**, 55–70.

deAzevedo, E.R., Bonagamba, T.J. and Schmidt-Rohr, K. (2000) *J. Magn. Reson.*, **142**, 86–96.

Detken, A., Hardy, E.H., Ernst, M., Kainosho, M., Kawakami, T., Aimoto, S. and Meier, B.H. (2001) *J. Biomol. NMR*, **20**, 203–221.

Egorova-Zachernyuk, T.A., Hollander, J., Fraser, N., Gast, P., Hoff, A.J., Cogdell, R., de Groot, H.J.M. and Baldus, M. (2000) *J. Biomol. NMR*, **19**, 243–253.

Ernst, R.R., Bodenhausen, G. and Wokaun, A. (1987) *Principles of Nuclear Magnetic Resonance in One and Two Dimensions*, Clarendon Press, Oxford.

Fu, R., Cotten, M. and Cross, T.A. (2000) *J. Biomol. NMR*, **16**, 261–268.

Griffin, R.G. (1998) *Nat. Struct. Biol.*, **5**, 508–512.

Gu, Z.T. and Opella, S.J. (1999a) *J. Magn. Reson.*, **138**, 193–198.

Gu, Z.T. and Opella, S.J. (1999b) *J. Magn. Reson.*, **140**, 340–346.

Hong, M. (1999) *J. Biomol. NMR*, **15**, 1–14.

Ishii, Y. and Tycko, R. (2000) *J. Am. Chem. Soc.*, **122**, 1443–1455.

James, F. and Ross, M. (1975) *Comput. Phys. Commun.*, **10**, 343–367. Internet address: http://wwwinfo.cern.ch/asdoc/minuit

Ketchem, R.R. and Cross, T.A. (1993) *Science*, **261**, 1457–1460.

Kovacs, F.A., Denny, J.K., Song, Z., Quine, J.R. and Cross, T.A. (2000) *J. Mol. Biol.*, **295**, 117–125.

Luca, S., Filippov, D.V., van Boom, J.H., Oschkinat, H., de Groot, H.J.M. and Baldus, M. (2001) *J. Biomol. NMR*, **20**, 325–331.

Marassi, F.M. (2001) *Biophys. J.*, **80**, 994–1003.

Marassi, F.M. and Opella, S.J. (2000) *J. Magn. Reson.*, **144**, 150–155.

Marassi, F.M., Gesell, J.J., Valente, A.P., Kim, Y., Oblatt-Montal, M., Montal, M. and Opella, S.J. (1999) *J. Biomol. NMR*, **14**, 141–148.

Marassi, F.M., Ma, C., Gesell, J.J. and Opella, S.J. (2000) *J. Magn. Reson.*, **144**, 156–161.

Marassi, F.M., Ramamoorthy, A. and Opella, S.J. (1997) *Proc. Natl. Acad. Sci. USA*, **94**, 8551–8556.

McDermott, A., Polenova, T., Bockmann, A., Zilm, K., Paulsen, E.K., Martin, R.W. and Montelione, G.T. (2000) *J. Biomol. NMR*, **16**, 209–219.

Middleton, D.A., Rankin, S., Esmann, M. and Watts, A. (2000) *Proc. Natl. Acad. Sci. USA*, **97**, 13602–13607.

Naito, A., Ganapathy, S., Akasaka, K. and McDowell, C.A. (1981) *J. Chem. Phys.*, **74**, 3190–3197.

Opella, S.J. (1997) *Nat. Struct. Biol.*, **4**, 845–848.

Opella, S.J., Marassi, F.M., Gesell, J.J., Valente, A.P., Kim, Y., Oblatt-Montal, M. and Montal, M. (1999) *Nat. Struct. Biol.*, **6**, 374–379.

Opella, S.J., Stewart, P.L. and Valentine, K.G. (1987) *Quart. Rev. Biophys.*, **19**, 7–49.

Palczewski, K., Kamasaka, T., Hori, T., Behnke, C.A., Motoshima, H., Fox, B.A., Le Trong, L., Teller, D.C., Okada, T., Stenkamp, R.E., Yamamoto, M. and Miyano, M. (2000) *Science*, **289**, 739–745.

Pauli, J., Baldus, M., van Rossum, B., de Groot, H. and Oschkinat, H. (2001) *ChemBioChem*, **2**, 272–281.

Pauli, J., van Rossom, B., Förster, H., de Groot, H.J.M. and Oschkinat, H. (2000) *J. Magn. Reson.*, **143**, 411–416.

Pines, A., Gibby, M.G. and Waugh, J.S. (1973) *J. Chem. Phys.*, **59**, 569–590.

Preusch, P.C., Norvell, J.C., Cassatt, J.C. and Cassman, M. (1998) *Nat. Struct. Biol.*, **5**, 13–14.

Ramamoorthy, A., Wu, C.H. and Opella, S.J. (1999) *J. Magn. Reson.*, **140**, 131–140.

Robyr, P., Tomaselli, M., Straka, J., Grob-Pisano, C., Suter, U.W., Meier, B.H. and Ernst, R.R. (1995) *Mol. Phys.*, **84**, 995–1020.

Russell, R.B. and Eggleston, D.S. (2000) *Nat. Struct. Biol.*, **7**, 928–930.

Schulte-Herbrüggen, T., Untidt, T.S., Nielsen, N.C. and Sørensen, O.W. (2001) *J. Chem. Phys.*, **115**, 8506–8517.

Shaka, A.J., Keeler, J. and Freeman, R. (1983) *J. Magn. Reson.*, **53**, 313–340.

States, D.J., Haberkorn, R.A. and Ruben, D.J. (1982) *J. Magn. Reson.*, **48**, 286–292.

Straus, S.K., Bremi, T. and Ernst, R.R. (1998) *J. Biomol. NMR*, **12**, 39–50.

Szeverenyi, N.M., Sullivan, M.J. and Maciel, G.E. (1982) *J. Magn. Reson.*, **47**, 462–475.

Tan, W.M., Gu, Z., Zeri, A.C. and Opella, S.J. (1999) *J. Biomol. NMR*, **13**, 337–342.

Teller, D.G., Okada, T., Behnke, C.A., Palezewski, K. and Stenkamp, R.E. (2001) *Biochemistry*, **40**, 7761–7772.

Teng, Q., Iqbal, M. and Cross, T.A. (1992) *J. Am. Chem. Soc.*, **114**, 5312–5321.

Tycko, R. (1996) *J. Biomol. NMR*, **8**, 239–251.

Unger, V.M., Hargrave, P.A., Baldwin, J.M. and Schertler, G.F.X. (1997) *Nature*, **389**, 203–206.

Wallin, E. and von Heijne, G. (1998) *Protein Sci.*, **7**, 1029–1038.
Wang, J., Denny, J., Tian, C., Kim, S., Mo, Y., Kovacs, F., Song, S., Nishimura, K., Gan, Z., Fu, R., Quine, J.R. and Cross, T.A. (2000) *J. Magn. Reson.*, **144**, 162–167.
Weiss, M.S. and Schulz, G.E. (1992) *J. Mol. Biol.*, **227**, 493–509.
Weiss, M.S., Abele, U., Weckesser, J., Welte, W., Schiltz, E. and Schulz, G.E. (1991) *Science*, **254**, 1627–1630.
Weliky, D.P. and Tycko, R. (1996) *J. Am. Chem. Soc.*, **118**, 8487–8488.
White, S.H. and Wimley, W.C. (1999) *Annu. Rev. Biophys. Biomol. Struct.*, **28**, 319–365.
Wishart, D.S. and Sykes, B.D. (1994) *Meth. Enzymol.*, **239**, 363–392.
Wu, C.H., Ramamoorthy, A., Gierasch, L.M. and Opella, S.J. (1995) *J. Am. Chem. Soc.*, **117**, 6148–6149.
Wu, C.H., Ramamoorthy, A. and Opella, S.J. (1994) *J. Magn. Reson. A*, **109**, 270–272.